Role of depolarizing GABAergic transmission for cortical network development

Dissertation
zur Erlangung des akademischen Grades

doctor rerum naturalium (Dr. rer. nat)

vorgelegt dem Rat der Medizinischen Fakultät
der Friedrich-Schiller-Universität Jena

von

Chuanqiang Zhang, M.Sc.

geboren am 05.01.1987 in Yueyang, China

1. Gutachter: PD Dr. Knut Kirmse

2. Gutachter: Prof. Dr. Otto W. Witte

3. Gutachter: Prof. Dr. Valentin Stein (Bonn)

Tag der öffentlichen Verteidigung: 02/07/2019

Inhalt

List of abbreviations

ACSF – artificial cerebrospinal fluid

AE3 – anion exchanger 3

AMPAR – α-amino-3-hydroxy-5-methyl-4-isoxazolepropionic acid receptor

AP – action potential

ATP – adenosine-5'-triphosphate

BBB – blood-brain barrier

CA1 – cornu amonis 1

CA3 – cornu amonis 3

$[Cl^-]_{in}$ – intracellular Cl^- concentration

CNS – central nervous system

Cre – recombinase enzyme

DF – driving force

E – embryonic day(s)

E_{Cl-} – Cl^- reversal potential

E_{GABA} – reversal potential of currents induced by GABA

E_{Glu} – reversal potential of currents induced by glutamate

Emx1 – gene encoding the protein empty spiracles homeobox 1

eNpHR3.0 – enhanced N. pharaonis halorhodopsin

GABA – gamma-amino-butyric acid

$GABA_AR$ – gamma-amino-butyric acid type A receptor

$GABA_BR$ – gamma-amino-butyric acid type B receptor

GCaMP3 – fusion protein consisting of green fluorescent protein, calmodulin and myosine light chain kinase peptide M13

GDPs – giant depolarizing potentials

HCO_3^- – bicarbonate

IEIs – inter-event intervals

IRES – internal ribosomal entry site

iso – isoguvacine

KCC2 – potassium-chloride co-transporter isoform 2

KO^{Emx1} – $Emx1^{IREScre}$ dependent knockout

LED – light-emitting diode

LFP – local field potential

loxP – locus of crossover in P1

mEPSCs – miniature AMPAR-mediated postsynaptic currents

mGPSCs – miniature $GABA_AR$-mediated postsynaptic currents

mPSCs – miniature postsynaptic currents

NKCC1 – sodium-potassium-chloride co-transporter isoform 1

NMDAR – N-methyl-D-aspartate receptor

P – postnatal day(s)

PSCs – postsynaptic currents

R_a – access resistance

R_{input} – membrane input resistance

R_{seal} – seal resistance

ROI – region of interest

sAP – spontaneous action potential

s.c. – subcutaneous injection

SEM – standard error of the mean

sGPSCs – spontaneous $GABA_AR$-mediated postsynaptic currents

sPSCs – spontaneous postsynaptic currents

SPWs – sharp waves

TTX – tetrodotoxin

V_m – membrane potential

WT – wild-type

Abstract

GABA mediates synaptic inhibition in the adult brain. However, in early development elevated intracellular Cl^- concentration ($[Cl^-]_{in}$) by NKCC1 causes $GABA_A$ receptor ($GABA_AR$) activation to be depolarizing in immature cortical neurons. Despite the potential promotion effect of depolarizing GABA for neuronal network development, a coherent picture cannot be drawn due to a lack of appropriate tools to manipulate the $[Cl^-]_{in}$ in the central nervous system (CNS). An Emx1-dependent conditional NKCC1 knockout mouse line which harbors disrupted NKCC1 function in cortical pyramidal cells and glia cells but leaving interneurons unaffected was used to explore the role of depolarizing GABAergic transmission on cortical network development. Optimized photo-stimulation of the optogenetic Cl^- pump eNpHR3.0 enables stable photo-currents, hence Cl^- loading, on longer time-scales. Next, combined with the optogenetic tool and patch-clamp techniques, the present work shows that NKCC1 contributes to GABAergic depolarization, and eNpHR3.0-mediated artificial loading of Cl^- in Emx1 positive cells contributes to the generation of spontaneous correlated network activity in the hippocampus *in vitro*. Disruption of NKCC1 function in Emx1 positive cells impairs such activity. However, this impairment is not due to an altered intrinsic excitability. In addition, the synaptic maturation is not affected in both GABAergic and glutamatergic synaptic transmission. The $GABA_AR$-mediated mGPSCs in cells from NKCC1 KO^{Emx1} animals undergo a normal developmental increase in frequency and acceleration in decay kinetics, while the AMPAR-mediated mEPSCs undergo a developmental increase in frequency and slowdown in decay kinetics. Three-dimensional voxel-based two-photon imaging revealed column-like Ca^{2+} clusters in visual cortex representing early spontaneous network activity. With the use of *in vivo* wide-field imaging technique, the present work shows that the deletion of NKCC1 in Emx1 positive cells does not affect the development of spontaneous network activity in the visual cortex, as the Ca^{2+} cluster frequency and cluster size undergo a developmental increase and they do not significantly differ between WT and NKCC1 KO^{Emx1} animals. In conclusion, NKCC1-mediated depolarizing action of GABA is not required for major aspects of cortical network development although it contributes to the generation of spontaneous network activity in the hippocampus *in vitro*.

Zusammenfassung

GABA vermittelt synaptische Hemmung von Neuronen im adulten Gehirn. In der frühen Entwicklung bewirkt eine erhöhte intrazelluläre Cl^- Konzentration ($[Cl^-]_{in}$) durch NKCC1, dass die Aktivierung des $GABA_A$ Rezeptors ($GABA_AR$) in unreifen kortikalen Neuronen depolarisierend wirkt. Obwohl der depolarisierende Effekt von GABA möglicherweise zur Reifung neuronaler Netzwerke beiträgt, ergibt sich aktuell kein kohärentes Bild. Hierfür fehlten bislang geeignete Instrumente zur Manipulation von $[Cl^-]_{in}$ im zentralen Nervensystem (ZNS). Eine Mauslinie mit einem konditionalen Knockout von NKCC1 unter der Kontrolle des Emx1 Promoters, die eine gestörte NKCC1 Funktion in kortikalen Pyramidenzellen und Gliazellen zur Folge hat, aber Interneurone unberührt lässt, wurde verwendet, um die Rolle der depolarisierenden GABAergen Übertragung für die Entwicklung des kortikalen Netzwerks zu untersuchen. Eine optimierte Photostimulation der optogenetischen Cl^- Pumpe eNpHR3.0 ermöglicht stabile Photoströme und damit Cl^- Beladung auf längeren Zeitskalen. Des Weiteren wird in der vorliegende Arbeit mithilfe optogenetischer Methoden und Patch-Clamp-Techniken nachgewiesen, dass NKCC1 zur GABAergen Depolarisation beiträgt und eine künstliche Beladung von Cl^- durch eNpHR3.0 in Emx1 positiven Zellen das Auftreten spontaner korrelierter Netzwerkaktivität im Hippocampus begünstigt. Die genetische Deletion von NKCC1 in Emx1 positiven Zellen beeinträchtigt diese Aktivität. Die Beeinträchtigung kann jedoch nicht auf eine veränderte intrinsische Erregbarkeit zurückgeführt werden. Darüber hinaus ist die synaptische Reifung sowohl für GABAerge als auch für glutamaterge Übertragung nicht betroffen. Die $GABA_AR$ vermittelten mGPSCs in Zellen von NKCC1 KO^{Emx1} Tieren durchlaufen einen normalen Entwicklungsanstieg der Frequenz und eine Beschleunigung der Abklingkinetik, während die AMPAR vermittelten mEPSCs einen Entwicklungsanstieg der Frequenz und eine Verlangsamung der Abklingkinetik erfahren. Die dreidimensionale voxel-basierte Zwei-Photonen-Bildgebung zeigte säulenartige Ca^{2+} Cluster, welche die frühe spontane Netzwerkaktivität im visuellen Kortex repräsentieren. Mittels In-vivo-Weitfeld-Bildgebung konnte in der vorliegenden Arbeit gezeigt werden, dass die Deletion von NKCC1 in Emx1-positiven Zellen die Entwicklung spontaner Netzwerkaktivität im visuellen Kortex nicht beeinflusst, da die Ca^{2+} Clusterfrequenz und Clustergröße einen Entwicklungsanstieg erfahren und sich nicht zwischen WT und NKCC1 KO^{Emx1} Tieren signifikant unterscheiden.

Zusammenfassend ist festzuhalten, dass die NKCC1-vermittelte depolarisierende Wirkung von GABA für wesentliche Aspekte der kortikalen Netzwerkentwicklung nicht erforderlich ist, obwohl sie *in vitro* zur Erzeugung der spontanen Netzwerkaktivität im Hippocampus beiträgt.

Acknowledgements

I would like to express my deepest thank to my mentor PD. Dr. Knut Kirmse. Thank you for all the excellent supervision and instruction, for the countless critical and constructive suggestions, for the enduring support to my research work and most importantly for the persistent inspiration. I have gained immense scientific knowledge and understanding to them to a level I could not achieve on my own. I have learned from you how to critically evaluate data from our own work and from others. I have learned so many things from you that I simply can´t list them here. I can´t thank you enough! Additionally, I would like to thank for the wonderful night for baking "Lebkuchen" together with your family. It was such a wonderful night, that I will never forget. Thank you, Knut!

I would like to express my sincere gratitude to Prof. Dr. Knut Holthoff. Thank you for co-supervising me, and for the many constructive suggestions. You have been always thinking critically but also positively. Your view of thinking questions is always surprising me. Leaving me to ask myself, why I have never thought questions in your way? Thank you for all of the encouraging and inspiring words! Many thanks to you for the warm reception and hospitality! It was my great honor!

I thank Prof. Dr. med. Otto W. Witte for his insightful comments on my work and support on various official issues. And thank you for organizing the big neurology department "summer pause" every year. I had a lot of fun at these events, delicious food, and dancing. I thank Prof. Dr. Christian A. Hübner for providing NKCC1$^{flox/flox}$ mouse line and discussion to some of the results. I thank Milena Zarkovic for explaining the approach has been used to create NKCC1$^{flox/flox}$ mouse line.

I thank Dr. John Dempster for customized modifying the Winfluor software, Marcel Schwittlick for kindly providing screencapturer code.

I thank Dr. Bernd Günther for his support on animal issues. I thank Frau Annett Ellinger, Frau Susette Lobert, Frau Angela Subarew, and Frau Jacqueline Klemm for their extensive work, professional care for multiple lines of experimental animals, and for always being very friendly.

I thank Frau Sindy Beck and Frau Ina Ingrisch for genotyping and technical assistance. I thank Frau Madlen Günther and Frau Claudia Sommer for Q-PCR data acquisition and analysis for my project, which is not included in the thesis. I thank Frau Svetlana Würl for kindly providing help.

I would like to thank all the current and previous colleagues, Dr. Michael Kummer, Dr. med. Alexander Jörk, Dr. Katja Krempler, Tom Floßmann, Jürgen Graf, Magdalena Aurelia Otto, Nicolas Witsch, Thomas Kaas, Niklas Langguth, Milena Günther, Anna Schaefgen. Thank you all for the friendly cooperation, funny small talks, Kajak excursion, BBQs, card games, and the very interesting “feuerzangenbowle”. Special thanks to Anna for those beautiful and delicious cakes and muffins, to Tom and Jürgen for their generous help in many aspects and interesting discussions over very broad topics. Thank you all! You guys make the BioImaging group be my surrogate family in Jena.

I thank Frau Nasim Kroegel for her generous help on all sorts of registration and documents. With her help, I was able to focus more on my research and have no concern of any official issues. I thank Dr. Anja Urbach, Dr. Silvio Schmidt, Dr. Christiane Frahm, Dr. Benedikt Grünewald, Dr. Marcus Böhme, and Steffen Kluckow for small talks and for getting me involved in all sorts of culturally interesting events.

I would also like to thank all of my friends with whom we spent some time together in Jena and sharing wonderful memories, Dr. Qian Chen, Biyun Zhang for taking German course together, Dr. Xiang Feng, Dr. Lun Yue, Jiacen Jiang, Fanhui Zeng for the nice tour in Croatia, Dr. Hongyong Wang and Xiao Shao for family like caring and delicious food, Tamar Chagunava and Najma Nabawi for hospitality, Maximilian Horn for the “Garden Grandpa” and Dr. Jingyu Liu, Yuanyuan Ji, Estelle Heyne for encouraging me and caring for me.

I thank my lovely Rock ’n’ Roll Tanzpartnerin Leonie Werner and Jenny Schmidt, with both of you I always feel very joyful (es macht sehr viel spaß! ☺). I thank my Rock ’n’ Roll teacher Herr Gernot Spangenberg and all dancing friends (especially Martina Hubáčková and Karl-Christian Böttcher) for the happy moments.

I would like to thank my family for taking care of me and being always supportive.

I dedicate this thesis to my parents.

Chapter 1. Introduction

The human brain comprises over 100 billion neurons, all of which have different morphologies and properties, and each neuron forms hundreds to thousands of connections to other neurons, thus building up an extremely complex network. In the adult brain, the information transfer between neurons is mainly mediated by excitatory and inhibitory neurotransmission. Glutamate is the main excitatory neurotransmitter and gamma-aminobutyric acid (GABA) is the main inhibitory neurotransmitter. Fast acting GABA inhibition works by opening $GABA_A$ receptors ($GABA_AR$) that are mainly permeable to Cl^-. Excitatory neurotransmitters are released by the pyramidal cells that account for around 80% of the neuronal population in cortex, whereas the inhibitory neurotransmitters are released mainly by the remaining 20% of the population called the interneurons (Hendry et al. 1987, Alfonsa 2015). Interestingly, *in vitro* investigations revealed a conserved developmental switch of the mode of GABA action from depolarization in immature neurons to hyperpolarization in mature neurons. The main question the thesis aimed to answer was: What is the role of depolarizing GABAergic transmission for cortical network development?

I will start by describing how GABAergic transmission-mediated inhibition works in the adult brain and how Cl^- regulation is such an important determinant for GABAergic activity. I will also introduce the current view of the principles underlying this ontogenetic development of GABA action. I will then review and discuss existing studies which explored the role of depolarizing GABA for cortical network development. In the end I will introduce the general approach and related techniques applied for addressing this question.

1.1 $GABA_AR$ and GABA induced inhibition

Pre-synaptically released GABA binds to its receptors in the postsynaptic cells and induces a conformational change in the receptors. GABA mainly affects two different types of receptors, namely ionotropic $GABA_AR$ and metabotropic $GABA_BR$. GABA mediated inhibition is to a large extent through activation of $GABA_AR$, which contain

five subunits and are mainly permeable to Cl^- and to a lesser extent to bicarbonate (HCO_3^-) (Bormann et al. 1987, Kaila et al. 1993).

From a mechanistic point of view, $GABA_AR$-dependent inhibition relies on two main mechanisms: I) voltage inhibition, which is due to the negatively charged Cl^- flowing into the cell, hence hyperpolarizing the membrane; II) shunting inhibition, which is due to the reduction of the membrane input resistance by $GABA_AR$ opening, making the cell membrane more "leaky" and thereby "short-circuiting" or counteracting (also requires Cl^- flowing into the cell) the incoming excitatory input to the cell, hence more excitation is needed to depolarize the cell according to Ohm's law (Kirmse and Holthoff 2017, Doyon et al. 2016, Spruston 2009). $GABA_AR$-mediated inhibition depends on the localization, affinity, and kinetics of $GABA_ARs$ and generally works in two modes: I) phasic inhibition (synaptic activation of $GABA_AR$, transient effect); II) tonic inhibition (extrasynaptic activation of $GABA_AR$, tonic effect, influences the basal excitability of the cell) (Kirmse and Holthoff 2017, Jacob et al. 2008).

The mode of GABA action through $GABA_AR$ activation is dependent on the driving force (DF_{GABA}), which is the difference between the membrane potential (V_m) and the reversal potential for currents induced by GABA (E_{GABA}).

$$DF_{GABA} = V_m - E_{GABA}$$

Since $GABA_AR$ are mainly permeable to Cl^-, E_{GABA} is to a large extent dependent on the intracellular Cl^- concentration ($[Cl^-]_{in}$). It should be noted that the $GABA_AR$ is also partially permeable to HCO_3^-. In mature neurons, the reversal potential for HCO_3^- (E_{HCO3-}) is around -10 mV. Since HCO_3^- is tightly connected with pH buffer mechanisms in both intracellular milieu and extracellular milieu, E_{HCO3-} is therefore relatively stable. However, despite taking the bicarbonate permeability into consideration, GABA is still often hyperpolarizing in mature neuron (in which $[Cl^-]_{in}$ is normally around 5 mM) as $GABA_AR$ is permeable to Cl^- 3.3-5 times more than to bicarbonate (Bormann et al. 1987, Kaila et al. 1993) (see Fig. 1B).

1.2 Cl^- regulation

The polarity of GABA currents strongly depends on Cl^- regulation of the postsynaptic cell that determines the E_{Cl-}. The main mechanism that sets basal $[Cl^-]_{in}$ has been considered to be the activity of co-transporters (Rivera et al. 1999, Yamada et al.

2004), but not intracellular impermeable anions (Dusterwald et al. 2018, Sulis Sato et al. 2017, Glykys et al. 2014). Neurons express different types of chloride-coupled co-transporters. The main importer of Cl^- is the sodium-potassium-chloride co-transporter (NKCC1) that brings $2Cl^-$ together with 1 potassium ion (K^+) and 1 sodium ion (Na^+) into the cell (Plotkin et al. 1997) (Fig. 1A). NKCC1 uses the driving force from Na^+ concentration gradient that is actively maintained to be low inside the cytosol by Na^+/K^+ ATPase (Pfeffer et al. 2009). When NKCC1 is at the thermodynamic equilibrium (which is usually not the case), then E_{Cl-} should be around –10 mV, which means under normal conditions NKCC1 action always mediates inward transport of Cl^- (Kirmse and Holthoff 2017). To extrude Cl^- on the other hand, neurons express the potassium-chloride co-transporter isoform 2 (KCC2) that brings a single Cl^- out of the membrane together with a single K^+, driven by the concentration gradient of K^+ that is high inside and low outside (Rivera et al. 1999). On top of these, neurons also express several types of sodium-chloride-bicarbonate co-transporters and anion exchangers (e.g. AE3, which normally accumulates Cl^- in exchange for intracellular bicarbonate and thereby raises intracellular Cl^- levels) that could also contribute to the basal $[Cl^-]_{in}$ (Pfeffer et al. 2009, Hübner and Holthoff 2013) (Fig. 1A). Various types of chloride channels are also involved in Cl^- regulation. Voltage-gated chloride channel ClC-2 constituting a substantial part of the background conductance, therefore under normal condition reduces excitability through shunting mechanism, while it helps to quickly dissipate chloride from neurons after chloride accumulation (Rinke et al. 2010, Ratte and Prescott 2011, Földy et al. 2010, Jentsch et al. 2002). It is also conceivable that hyperpolarizing $GABA_AR$-mediated responses involve Cl^- influx which, in turn, reduces DF_{GABA}. This reduction of DF_{GABA} or change of $[Cl^-]_{in}$ is much more pronounced for neurons that are involved in a network activity. Glutamatergic activity exerts a strong depolarization in a neuron that brings its V_m towards reversal potential of currents induced by glutamate (E_{Glu}), which is around 0 mV. This, in turn, creates a huge driving force for Cl^- influx when the conductance is increased by the opening of $GABA_ARs$ (Buzsaki et al. 2007). Although neurons are equipped with Cl^- extrusion mechanism such as KCC2 that will clear Cl^- back towards its initial $[Cl^-]_{in}$, but this process is not as fast as synaptic events (Jin et al. 2005). Intense network activity may, therefore, cause a rapid increase of $[Cl^-]_{in}$ thus reducing the DF_{GABA} and even sometimes results in a switch of

GABA polarity from hyperpolarizing to depolarizing in a mature neuron (Alfonsa 2015, Stein and Nicoll 2003, Gulledge and Stuart 2003).

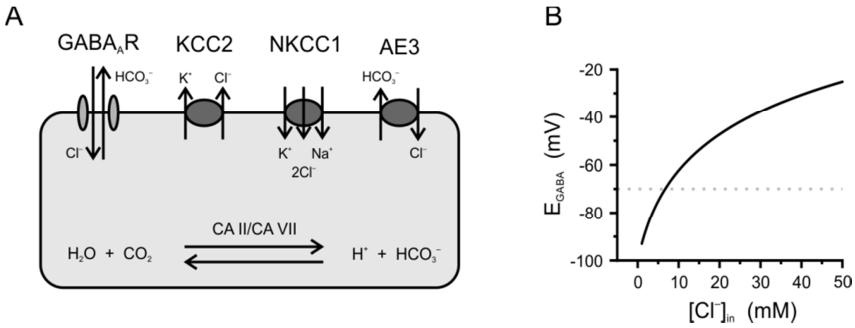

Figure 1. Cl^- regulation and E_{GABA}. A, $[Cl^-]_{in}$ regulation related proteins. $GABA_AR$ are permeable to Cl^- and HCO_3^-, with a permeability ratio P_{Cl-}/P_{HCO3-} of around 3.3-5. Electroneutral potassium-chloride co-transporter KCC2 mediates chloride extrusion in mature neurons. Electroneutral sodium-potassium-chloride co-transporter NKCC1 mediates Cl^- uptake in immature neurons. Electroneutral anion exchanger mediates Cl^- uptake and is involved in pH regulation. HCO_3^- is tightly linked to alterations of pH. B, E_{GABA} plotted against $[Cl^-]_{in}$, taking HCO_3^- permeability and constant E_{HCO3-} into consideration (assuming P_{HCO3-} equals 0.2, and $[HCO_3^-]_{out}$ equals 26 mM, $[HCO_3^-]_{in}$ equals 16 mM, temperature at 37 ^oC, dotted horizontal line indicate V_m at –70 mV).

1.3 Developmental shift of GABA action

Neuronal Cl^- regulation changes throughout development. In immature neurons, the $[Cl^-]_{in}$ is found to be higher compared to the mature neuron (Yamada et al. 2004). This is consistent with the tendency of $GABA_AR$ activation to give an outward flow of Cl^-, hence exerting a depolarizing effect, in immature neurons. On the other hand, in mature neurons $[Cl^-]_{in}$ is maintained low that consequently results in a hyperpolarizing effect of GABA (Rivera et al. 1999). These $[Cl^-]_{in}$ differences could be explained by the developmental up-regulation of KCC2 that is part of neuronal differentiation during maturation (Rivera et al. 1999). Immature neurons dominantly express NKCC1 over KCC2, however, as the neurons mature KCC2 is drastically up-regulated while NKCC1 is only slightly if at all up-regulated (Kirmse and Holthoff 2017, Kang et al. 2011), explains the developmental shift from depolarizing GABA towards hyperpolarizing GABA (Kirmse et al. 2011, Stein et al. 2004).

1.4 The role of depolarizing GABA in development

The formation of the neuronal circuitry is first instructed by molecular interactions, which are controlled by genetic programs, and later, during a prolonged period, refined by neuronal activity. Apart from sensory triggered neuronal activity, the neuron network generates spontaneous activity during early development (Khazipov and Luhmann 2006, Luhmann et al. 2016). Data obtained from *in vitro* preparations suggest that the depolarizing action of GABA is excitatory and is instrumental in generating some forms of early neocortical network activity since they can be blocked acutely by the NKCC1 antagonist bumetanide (Allene et al. 2008, Rheims et al. 2008). In the hippocampus during the first postnatal week, GABA-mediated depolarization drives activity across groups of neurons, giving rise to correlated network events known as giant depolarizing potentials (GDPs) (Khalilov et al. 1999). In somatosensory cortex, at the end of the first postnatal week, GABA-driven cortical GDPs repetitively synchronize localized neuronal assemblies (Allene et al. 2008). At present, however, supportive evidence from *in vivo* studies for a contribution of depolarizing GABA to the generation of network activity is virtually lacking, except (Sipilä et al. 2006). What are the developmental functions of a depolarizing, rather than hyperpolarizing, mode of GABA action in early life? To understand the developmental functions of depolarizing GABA, genetic as well as pharmacological approaches were applied for targeting NKCC1 in different studies. In immature mouse neocortex, abolishing GABA-mediated depolarization by systemic administration of the NKCC1 antagonist bumetanide from embryonic day (E) 15 to postnatal day (P) 7 disrupted excitatory synapse formation permanently as measured by miniature postsynaptic currents, and altered the morphology of cortical neurons as bumetanide-treated cells had significantly decreased dendrite length, dendrite volume, branch levels, branch points, number of dendrite segments, and terminal points (Wang and Kriegstein 2011). Whereas systemic bumetanide application (P3–7) in rats led to a moderate prolongation of ocular dominance plasticity, which was accompanied by a selective delay in the maturation of GABAergic synaptic transmission, but the development of glutamatergic contacts, dendritic morphology, and visual capabilities remained unaffected (Deidda et al. 2015). However owing to a low blood-brain barrier (BBB) permeability of bumetanide (Wang et al. 2015, Brandt et al. 2010), it remains unclear whether above described effects are causally related

to an attenuation of cortical GABAergic depolarization. As for a genetic approach, two groups have independently used transgenic mouse models, in which the NKCC1-encoding gene *Slc12a2* was knocked out to produce a homozygous NKCC1-null ($NKCC1^{-/-}$) mutant (Pfeffer et al. 2009, Sipilä et al. 2009). The Hübner group found that, in hippocampal pyramidal cells, NKCC1 deletion attenuated GABAergic depolarization in neonates, impaired the generation of GDP-like activity, and delayed the functional maturation of both GABAergic and glutamatergic synapses as revealed by electrophysiological measurement of miniature postsynaptic currents. However, unlike previous work in cortical neurons, the reduction in GABAergic depolarizing driving force did not impede the morphological maturation of dendrites in the hippocampal cells (Pfeffer et al. 2009). The Kaila group found that NKCC1 deletion led to an almost complete loss of GABA induced depolarization, but bursts of GDP-like events were also found in $NKCC1^{-/-}$ cells, with a mean frequency, amplitude, and duration comparable to those of wild-type (WT) GDPs. These bursts of GDP-like events in the $NKCC1^{-/-}$ hippocampal network were generated due to a compensatory enhancement of intrinsic neuronal excitability (Sipilä et al. 2009). Despite deviating in some key observations, these two knockout studies showed that NKCC1 may not always be essential for the maturation of excitatory synapses or the proper morphology of dendrites (Wright 2009). However, the severe phenotype (including deafness, imbalance and premature death) of these mice, which is related to non-cortical NKCC1 deletion, seriously constrains their use as a model system for developmental studies (Delpire et al. 1999). The observations are thus subjected to alternative interpretations (Löscher et al. 2013). Due to these methodological limitations, currently, a coherent picture of the role of depolarizing GABA in the immature brain cannot be drawn.

1.5 Optogenetic inhibition with Cl^- pump eNpHR3.0

In recent years, optogenetic tools for reversible silencing of neurons became an integral component of experimental neuroscience. They facilitate analyzing how distinct neuronal populations causally contribute to brain dynamics at the cellular, network and behavioral level and, in addition, promise substantial therapeutic potential in diverse clinical contexts (Bui et al. 2017, Klapper et al. 2016, Moser 2015). Optogenetic tools for neuronal inhibition are molecularly diverse, including

light-activated Cl^- channels (Wietek et al. 2015, Berndt et al. 2016), G-protein-coupled receptors (Siuda et al. 2015, Masseck et al. 2014) and ion pumps (Zhang et al. 2007, Gradinaru et al. 2010, Chow et al. 2010). All actuators developed so far have specific biophysical constraints that are of practical interest when designing and interpreting experimental studies and data, respectively (Wiegert et al. 2017). For example, light-gated Cl^- channels enable divisive inhibition by shunting excitatory currents, but the direction of ion flow entirely depends on the existing electrochemical Cl^- gradient and, consequently, may also depolarize rather than hyperpolarize cells (Mahn et al. 2016, Szabadics et al. 2006, Price and Trussell 2006). Light-activated G protein-coupled receptors operate on slower timescales and modulate intracellular signaling cascades and therefore could lead to undesired off-target effects in addition to reducing excitability (Kim et al. 2005, Airan et al. 2009). In contrast, light-driven ion pumps exhibit on-/off-kinetics in the millisecond range and employ subtractive inhibition, which renders them virtually independent of existing electrochemical gradients (Zhang et al. 2011). A widely used inhibition pump is eNpHR3.0 (Gradinaru et al. 2010), an improved version of the light-driven Cl^- pump halorhodopsin derived from Natronomas pharaonis (Zhang et al. 2007). A critical constraint of eNpHR3.0 results from its prominent inactivation, i.e. a decline in photo-current amplitude during continuous illumination (Alfonsa et al. 2015, Mattis et al. 2012, Tonnesen et al. 2009, Zhang et al. 2007, Han and Boyden 2007). Inactivation has a time constant in the range of seconds implying limited usability of eNpHR3.0 in experimental settings that require long-lasting (>10 s) inhibition, for review see (Wiegert et al. 2017). Based on data obtained from structurally related halorhodopsins, inactivation is thought to result from a branched photo-cycle with an accumulation of intermediates containing a deprotonated Schiff base in the 13-cis-retinal configuration (Bamberg et al. 1993). The return to the initial state, which involves thermal reversion to all-trans-retinal, is slow but can be accelerated by short-wavelength visible light (Zhang et al. 2007, Han and Boyden 2007). Since eNpHR3.0-mediated photo-current is due to Cl^- being pumped into the cell, a novel use of eNpHR3.0 is, therefore, for chloride loading.

Chapter 2. The objectives of this thesis

2.1 Part 1 [1]

Light-driven ion pumps are important tools for silencing neuronal populations in a cell type-specific manner. One of the most widely used inhibitory optogenetic actuators is the Cl^- pump eNpHR3.0. However, due to a pronounced decline of photo-current amplitudes during continuous illumination, the use of eNpHR3.0 is limited in situations that prolonged inhibition was required.

The main objective was to optimize the stimulation regime to improve the temporal stability of eNpHR3.0-mediated photo-currents during long-term photo-stimulation, in order to enable applications to situations in which long-lasting inhibition of neuronal activity is required. Consequently, this would enhance the capability of eNpHR3.0 for Cl^- loading during prolonged periods.

2.2 Part 2 [2]

In early development, elevated $[Cl^-]_{in}$ causes $GABA_A$ receptor activation to be depolarizing in immature cortical neurons. It has been hypothesized that depolarizing GABA might play a crucial role in the generation of early spontaneous correlated network activity and hence affects the maturation of cortical networks by promoting synaptogenesis. In order to examine the role of depolarizing GABA for cortical network development, a cre-loxP-based transgenic mouse model was used, which harbors a conditional deletion of the major Cl^- importer NKCC1 in the vast majority of forebrain glutamatergic cells. This approach circumvents the effects of peripheral NKCC1 disruption.

[1] Results, text and figures of Part 1 have been modified and extended on the basis of a manuscript that is currently under preparation. For details regarding author contributions, please see "Ehrenwörtliche Erklärung".

[2] Results, text and figures of Part 2 have been published (Kummer et al. 2016) or modified and extended on the basis of a manuscript that is currently under preparation. For details regarding author contributions, please see "Ehrenwörtliche Erklärung".

Specific objectives are:

(1) to examine the role of NKCC1 in maintaining the depolarizing effect of GABA

(2) to explore how NKCC1-dependent Cl^- uptake contributes to the maturation of intrinsic excitability and synaptic properties

(3) to investigate as to which extent the expression of NKCC1 by pyramidal cells promotes the generation of spontaneous correlated activity.

Chapter 3. Methods

3.1 Ethics statement

All experimental procedures were carried out with approval from the local government (registration number: 02-053/11, Thüringer Landesamt für Verbraucherschutz) and complied with European Union norms (Directive 2010/63/EU).

3.2 Animals

In general Cre-loxP system was used to achieve cell-type specific deletion of certain gene or genes (Austin et al. 1981). Several commercially available mouse lines were used: *Emx1*^{IREScre} strain (The Jackson Laboratory, stock no. 005628) (Gorski et al. 2002), *Ai39* cre-reporting strain (The Jackson Laboratory, stock no. 014539) (Madisen et al. 2012) and *Ai*38 cre-reporting strain (The Jackson Laboratory, stock no. 014538) (Zariwala et al. 2012) and in addition a non-commercial NKCC1$^{flox/flox}$ strain (kindly provided by Christian A. Hübner, Institute for Human Genetics, Jena) (Antoine et al. 2013).

Emx1^{IRESCre} knockin mice (https://www.jax.org/strain/005628) have the endogenous Emx1 locus directing expression of Cre recombinase in pyramidal cells and glia cells of neocortex and hippocampus, but not in GABAergic interneurons (Kummer et al. 2012).

Ai39 mouse contains Rosa-CAG-LSL-eNpHR3.0-EYFP-WPRE conditional allele, a loxP flanked STOP cassette prevents transcription of the downstream eNpHR3.0-EYFP fusion gene. The CAG promoter driven reporter construct was targeted for insertion into the Gt(ROSA)26Sor and eNpHR3.0-EYFP expression is determined by which tissue(s) express Cre recombinase (https://www.jax.org/strain/014539).

Ai38 mouse contains Rosa-CAG-LSL-GCaMP3-WPRE conditional allele, a loxP flanked STOP cassette prevents transcription of the downstream GCaMP3 (Ca^{2+} indicator) fusion gene. The CAG promoter driven reporter construct was targeted for insertion into the Gt(ROSA)26Sor locus and GCaMP3 expression is determined by which tissue(s) express Cre recombinase (https://www.jax.org/strain/014538).

In NKCC1$^{flox/flox}$ mice, exons 8-10 of the *Slc12a2* gene are flanked by loxP sites. The disruption of NKCC1 protein expression is determined by which tissue(s) express Cre recombinase.

Optogenetic related experiments were performed on acute brain slices prepared from mice of both sexes at postnatal day (P) 4–13. Pyramidal cell-specific expression of an eNpHR3.0-EYFP fusion protein was achieved by crossing homozygous female *Emx1^{IREScre}* mice (Gorski et al. 2002) to homozygous male mice of the *Ai39* cre-reporting strain (Madisen et al. 2012).

NKCC1$^{flox/flox}$ strain was used in combination with Emx1^{IREScre} strain to achieve early embryonic cell-type specific NKCC1 knockout (Antoine et al. 2013), leaving GABAergic interneurons unaffected while disrupting NKCC1 expression in cortical and hippocampal glutamatergic neurons and glia cells.

NKCC1 related experiments were performed either on Emx1$^{IREScre/wt}$:NKCC1$^{flox/flox}$ mice (hereafter denoted as NKCC1 KO^{Emx1}) or on Emx1$^{wt/wt}$:NKCC1$^{flox/flox}$ mice (hereafter denoted as NKCC1 WT), which were obtained by crossing female Emx1$^{IREScre/wt}$:NKCC1$^{flox/flox}$ mice to male Emx1$^{wt/wt}$:NKCC1$^{flox/flox}$ mice. When GCaMP3 signal is needed for measuring activity optically, experiments were performed either on Emx1$^{IREScre/wt}$:GCaMP3^{LSL}:NKCC1$^{flox/flox}$ (GCaMP3 NKCC1 KO^{Emx1}) mice or on Emx1$^{IREScre/wt}$:GCaMP3^{LSL}:NKCC1$^{wt/wt}$ (GCaMP3 NKCC1 WT) mice. These mice were obtained by crossing female Emx1$^{IREScre/IREScre}$:NKCC1$^{flox/wt}$ mice to male GCaMP3$^{LSL/LSL}$:NKCC1$^{flox/wt}$ mice.

3.3 Preparation of acute brain slices

Animals were decapitated under deep isoflurane anesthesia. The brain was removed quickly and transferred into ice-cold saline containing (in mM): 125 NaCl, 4 KCl, 10 glucose, 1.25 NaH_2PO_4, 25 $NaHCO_3$, 0.5 $CaCl_2$, and 6 $MgCl_2$, bubbled with 5% CO_2 / 95% O_2 (pH, 7.4). Horizontal brain slices containing the hippocampus (350 µm) or coronal brain slices (350 µm) comprising the occipital cortex were cut on a vibratome and stored for at least 1h before their use in artificial cerebrospinal fluid (ACSF) containing (in mM): 125 NaCl, 4 KCl, 10 glucose, 1.25 NaH_2PO_4, 25 $NaHCO_3$, 2 $CaCl_2$, and 1 $MgCl_2$, bubbled with 5% CO_2/95% O_2 (pH, 7.4). During incubation, the temperature of ACSF in incubation chamber passively drops down from 32-34°C to

room temperature. For recordings, slices were placed into a submerged-type recording chamber on the microscope stage (Nikon Eclipse FN1, Nikon Instruments Inc.) equipped with near-infrared differential interference contrast optics (ACSF flow rate ~3 ml min^{-1}). Experiments were performed at near physiological temperature (32-34°C).

3.4 Optogenetic stimulation

Excitation was provided by a 488 nm diode laser (Cobolt MLD 488) and a 594 nm solid-state laser (Cobolt Mambo), intensity-modulated by an acousto-optic tunable filter (GH18A, Gooch & Housego) and coupled into a multimode 0.22 NA optical fiber with a core diameter of 200 µm (FG200LCC, Thorlabs GmbH). The tip of the fiber was positioned at an axial distance of ~0.5 mm to the patched cell in CA1 pyramidal layer, closely to the surface of the slice. All power levels indicated were calibrated at the fiber tip, separately for each wavelength (LabMax-TO with OP-2 VIS sensor, Coherent). Photo-stimulation of eNpHR3.0 was performed using either continuous or high-frequency pulse-like (1 kHz, on/off 20/80%) stimulation patterns. The on/off time constant of the acousto-optic tunable filter was ≤6 µs, as quantified using a fast photodiode (PDA100A, Thorlabs).

3.5 Puff application

TTL signal triggered puff application of isoguvacine (100 µM) at a nominal pressure of 10 psi (100 ms or 2 seconds) was performed via a patch pipette (tip diameter, ~2.5 µm) positioned in the vicinity of the recorded cell. Substances for application were dissolved in the extracellular solution of the respective control condition.

3.6 Electrophysiological measurements

3.6.1 eNpHR3.0 related recordings

Electrophysiological signals were acquired using a Multiclamp 700B amplifier, a 16-bit AD/DA board (Digidata 1550A) and the software pClamp 10 (Molecular Devices). Signals were low-pass filtered at 3 kHz and sampled at 10 kHz (or 20 kHz when

necessary). For patch-clamp recordings from CA1 pyramidal cells, glass pipettes (4–7 MΩ) were filled with the following solution (in mM): 40 KCl, 100 K^+-Gluconate, 1 $CaCl_2$, 11 EGTA, 10 HEPES, 2 Mg^{2+}-ATP, 0.3 Na^+-GTP (pH adjusted to 7.25 with KOH). Whole-cell voltage-clamp recordings were performed at a holding potential of –70 mV. In whole-cell current-clamp measurements, the resting membrane potential was manually biased to about –65 mV via current injection. Voltages were not corrected for liquid junction potentials (LJP). A blue-light pulse (488 nm, 3 s, 5 mW) was routinely applied (except for experiments illustrated in Fig. 2A-B) at the end of each stimulation trial to accelerate the recovery of eNpHR3.0-mediated currents from inactivation (for an example see Fig. 4*A*). The recovery from inactivation of eNpHR3.0-mediated currents (Fig. 2C) was fitted, separately for each cell, by a mono-exponential function of the following form:

$$recovery\ (\%) = a * e^{-\Delta t/\tau} + c$$

where Δt is the latency of the test pulse onset, τ is the recovery time constant, the offset c was constrained to 100%.

Due to a high intercellular variability of input resistances, the amplitude of injected currents used to evoke action potential (AP) firing in current-clamp experiments (see Fig. 5) was separately set for each cell and kept constant throughout the recording. Using a series of repetitive current injections (1 s, 5 pA increments), the amplitude was determined from the largest current step that failed to induce APs under brief (2 s, 5 mW) photo-stimulation at 488 nm.

3.6.2 NKCC1 related recordings

Experiments were blinded to genotype. Electrophysiological signals were acquired using an Axopatch 200B (patch-clamp) or Multiclamp 700B (patch-clamp and extracellular recordings) amplifier, a 16-bit AD/DA board (Digidata 1440A or Digidata 1550A) and pClamp 10 (Molecular Devices). Signals were either low-pass-filtered at 1-3 kHz and sampled at 10-20 kHz in patch-clamp studies or low-pass-filtered at 6 kHz and sampled at 20 kHz in extracellular recordings. To non-invasively estimate Cl^- reversal potential, GABA-induced membrane potential (V_m) alteration was measured by using low concentration gramicidin perforated current-clamp recordings (I = 0 mode of the amplifier) (Perkins 2006, Mason et al. 2005). Recording pipettes (5–8 MΩ) were filled with the following solution (in mM): 140 K-gluconate, 1 CaCl2, 2 MgCl2, 11 EGTA, 10 HEPES (pH 7.25 with KOH), containing additional 40–80 µg/ml

gramicidin. LJP was calculated by using pClamp 10 (Barry and Lynch 1991). Voltages were corrected for LJP (~16 mV).

For measurements of spontaneous action currents or agonist-induced action currents tight-seal cell-attached recordings were performed in the voltage-clamp mode using glass pipettes filled with the following solution (in mM): 150 NaCl, 4 KCl and 10 HEPES (pH 7.4), in addition Alexa 555 (50 µM) was added into pipette solution to identify possible breakthrough and for morphological identification after recording. Holding current was manually zeroed before each experiment.

$GABA_A$R-mediated spontaneous postsynaptic currents (sGPSC) were recorded using the whole-cell configuration of the patch-clamp technique. Intra-pipette solution (in mM): Cs-methansulfonat 150, NaCl 5, HEPES 10, EGTA 5, $CaCl_2$ 0.5, pH 7,3 adjusted with CsOH. Calculated LJP is 10 mV. This was compensated during recording by setting the nominal holding potential to 10 mV (so that membrane potential of the cell is hold at 0 mV). No synaptic blocker was applied, sGPSC were isolated from glutamatergic postsynaptic currents by the holding potential. sGPSC were detected by template matching procedure in Clampfit. To quantify sGPSC bursts, the fraction of inter-sGPSC intervals (IEIs) ≤ 50 ms was introduced and defined as burst index. Burst index is highly dependent on sGPSC frequency. To help the interpretation, calculated burst indices from recordings were compared to analytical values obtained by assuming a stochastic occurrence of sGPSCs.

Suppose that sGPSC events appear stochastically, then the number of events k in an interval follows a Poisson distribution with the probability mass function:

$$P(k) = \frac{\lambda^k * e^{-\lambda}}{k!}$$

in which λ is the mean event rate (https://en.wikipedia.org/wiki/Poisson_distribution). Define T as time to the first event. Then the probability of T being smaller than or equal to a defined time period t can be expressed as:

$$P(T \leq t) = 1 - P(T > t) = 1 - P(N = 0 \; in \; t \; interval)$$

According to Poisson distribution probability mass function (in t interval)

$$P(T \leq t) = 1 - \frac{(\lambda t)^0 * e^{-(\lambda t)}}{0!} = 1 - e^{-\lambda t}$$

Hence, if the number of events follows a Poisson distribution with λ as mean rate, then inter-event intervals are exponentially distributed. The probability of an event within a time t is given by:

$$P(T \leq t) = 1 - e^{-\lambda t}$$

According to the above definition of burst index (fraction of IEIs ≤ 50 ms), burst index at different mean rates λ equals:

$$Burst\ Index(\lambda) = 1 - e^{-\lambda t}$$

where λ is event frequency (in Hz) and t set to 0.05 s.

Spontaneous postsynaptic currents (sPSC) were recorded using the whole-cell configuration of the patch-clamp technique. Intra-pipette solution (in mM): 40 KCl, 100 K^+-Gluconate, 1 $CaCl_2$, 11 EGTA, 10 HEPES, 2 Mg^{2+}-ATP, 0.3 Na^+-GTP (pH adjusted to 7.25 with KOH). Recordings were performed at a holding potential of –70 mV. Voltages were not corrected for LJP. sPSC bursts were detected visually with following criteria: I) > 400 ms in duration II) > 200 pA in amplitude.

To measure the passive properties and intrinsic excitability whole-cell current-clamp technique was applied. Intra-pipette solution contained (in mM): NaCl 150, KCl 4, HEPES 10, (pH 7.4). Membrane potential was corrected for LJP (calculated to be –15 mV) during analysis. Holding potential was set to −70 mV. Access resistance was monitored by applying hyperpolarizing pulses of 10 mV. Passive properties were extracted from the capacitance artifacts as well. Responses of neurons to 500 ms episodic current injections from -120 pA to 120 pA with 10 pA increments were recorded.

$GABA_A$R-mediated postsynaptic miniature currents (mGPSCs) and AMPAR-mediated postsynaptic miniature currents (mEPSCs) were recorded using the whole-cell configuration of the patch-clamp technique. Intra-pipette solution contained (mM): (1) for mGPSCs: CsCl 145, NaCl 5, HEPES 10; QX-314 2, EGTA 0.2, Mg-ATP 2; Na-GTP 0.3 (pH 7.3 with CsOH) (2) for mEPSCs: Cs-methanesulfonate 125, CsCl 20, NaCl 5, HEPES 10; QX-314 2, EGTA 0.2, Mg-ATP 2; Na-GTP 0.3 (pH 7.3 with CsOH). For morphological identification, intra-pipette solution additionally contained 50 µM Alexa 555. Pipette resistance was 3–5 MΩ, when filled with the above saline. Voltages were not corrected for LJP. Holding potential was set to −70 mV, if not otherwise mentioned. Access resistance was monitored by applying hyperpolarizing pulses of 10 mV. According to Ohm´s law, access resistance was calculated by dividing 10 mV with measured capacitance artifact´s peak value. Only recordings with an access resistance below 30 MΩ were accepted. Series resistance compensation was not applied.

Extracellular recordings (under *in vivo* condition) were performed using glass pipettes beveled to a resistance of 200–500 KΩ. Recording pipettes filled with ACSF were positioned in the upper cortical plate under two-photon guidance. For synchronization with wide-field Ca^{2+} imaging recording, a red light-emitting diode (LED) was used to deliver 10-ms light pulses at the beginning and the end of the recording.

3.7 Surgical preparation

For *in vivo* recordings, animals were deeply anesthetized with isoflurane (3.5% for induction, 1–2% for maintenance) in pure oxygen and the skin overlying the skull was locally infiltrated with 2% lidocaine (s.c.). A heating pad (set at 35 $^{\circ}$C) was used to maintain the body temperature of the animal. When breathing rate reached around 50 breaths min^{-1}, the skin was cut by using a fine scissors. After that the isoflurane concentration was adjusted to keep the breathing rate to around 100 breaths min^{-1}. Scalp and periosteum were carefully removed, and a plastic chamber with a central hole (Ø 2–4 mm) was fixed on the skull using cyanoacrylate glue (Kummer et al. 2012, Garaschuk et al. 2006). The recording chamber was tightly connected to the microscope stage and subsequently perfused with ACSF containing (in mM): 125 NaCl, 4 KCl, 25 $NaHCO_3$, 1.25 NaH_2PO_4, 2 $CaCl_2$, 1 $MgCl_2$ and 10 glucose (pH = 7.4 at 35–36 $^{\circ}$C; ACSF flow rate ~3 ml min^{-1}). A craniotomy was performed above the left occipital cortex by scratching with a tip bent 27G needle. Care was taken not to damage the underlying dura mater.

3.8 Anesthesia and animal monitoring during recordings

During *in vivo* recordings, body temperature was continuously monitored and maintained at close to physiological values (34–37 °C) by means of a heating pad. Spontaneous respiration was monitored using a differential pressure amplifier (Spirometer Pod and PowerLab 4/35, ADInstruments).

For recordings, isoflurane was discontinued after completion of the surgical preparation and gradually substituted with the analgesic-sedative nitrous oxide (up to the fixed final N_2O/O_2 ratio of 3:1). Experiments started ≥ 90 min after withdrawal of isoflurane.

3.9 Three-dimensional two-photon microscopy

Voxel imaging was performed using a Movable Objective Microscope (Sutter Instrument) equipped with two galvanometric scan mirrors (6210H, MicroMax 673XX Dual Axis Servo Driver, Cambridge Technology) and a piezo focusing unit (P-725.4CD PIFOC, E-665.CR amplifier, Physik Instrumente) controlled by custom-made software written in LabVIEW 2010 (National Instruments) (Kummer et al. 2016, Kummer et al. 2015). Voxel imaging was based on a spiral-shaped trajectories scanning. To achieve that, a previously used approach has been adapted (Göbel et al. 2007) which combines galvanometric lateral (X–Y) scanning with sinusoidal piezo actuator-driven objective movements along the Z-axis (Kummer et al. 2015). Scanning trajectories used in the present study comprised equidistant scan points (~0.9 µm) (Kummer et al. 2016, Kummer et al. 2015). Fluorescence excitation at 920 nm was provided by a tunable Ti:Sapphire laser (Chameleon Ultra II, Coherent) using a 20×/1.0 NA water immersion objective (XLUMPLFLN 20XW, Olympus). Emission light was separated from excitation light using a 670-nm dichroic mirror (670 DCXXR, Chroma Technology), short-pass filtered at 680 nm and detected by a photomultiplier tube (H10770PA-40, Hamamatsu). Data were acquired using two synchronized data acquisition devices (NI 6110, NI 6711, National Instruments).

3.10 Wide-field epifluorescence microscopy

One-photon excitation of the genetically encoded Ca^{2+} indicator GCaMP3 was provided by a xenon arc lamp (Lambda LS, Sutter Instrument) coupled via a liquid light-guide to the epifluorescence port of a Movable Objective Microscope (Sutter Instrument) and filtered at 472/30 nm. Emission was separated from excitation light at 495 nm and long-pass-filtered at 496 nm (AHF Analysentechnik). Images were acquired using a 10×/0.3 NA water immersion objective (Zeiss) and a 12 bit Rolera-XR camera (QImaging) operated by the software Winfluor (written by J. Dempster, University of Strathclyde, Glasgow, UK) or Streampix 5 (NorPix). Frame rate was set to 74.3 Hz using 4 × 4 hardware binning (170 × 130 pixels; field of view: 1134 × 867 mm). Recording time per animal typically amounted to ~20 min.

For analysis, periods of movement artifacts were first identified by visual inspection of raw image sequences and discarded since they frequently resulted in obviously false-positive detection results. Images were then binned (10 × 10), giving rise to a regular grid of 17 × 13 = 221 ROIs (region of interest, ROI dimensions: 66.7 × 66.7 mm). Next, intensity-versus-time plots were extracted using ImageJ 1.47 (http://imagej.nih.gov/ij/). Unbiased peak detection of spontaneous calcium transients (CaTs) was performed using a template-matching algorithm implemented in pClamp 10. 'Clusters' of CaTs peaks were defined on a temporal basis as follows. Extracted peak times were binned (bin width = 10 frames, ~130 ms) and neighboring non-empty bins (that is, bins with ≥ 1 peak) were considered to belong to a common temporal cluster if they were separated by less than two empty bins. The mean frequency of CaTs per ROI and the mean cluster frequency were calculated as the ratio of the number of events per corrected recording time (that is, total recording time minus cumulative movement artifact-associated recording time).

3.11 Fluorescence based identification of Emx1^{IREScre} positive cells

When GCaMP3 or eNpHR3.0-EYFP is expressed in Emx1^{IREScre} positive cells, fluorescence signal can be used for identification of these cells. Fluorescence signals were acquired using a CSU10 Nipkow-disc scanning unit in combination with a high spatial resolution RoleraXR camera driven by the software Winfluor or QCapture Pro 6 (QImaging). Excitation light at 488 nm was provided by a single wavelength solid-state laser Sapphire CDRH-LP (Coherent). In CSU10 unit, a dichroic mirror (Yokogawa CSU-HC T405-488, AHF) and an emission filter (RazorEdge LP 488 RE, AHF) were installed.

3.12 Genotyping

After experiment, tissue samples from tail, cortex, and small intestine were obtained for genotyping. The rationale is that Emx1^{IREScre} recombinase activity is absent from small intestine tissue (therefore serve as a negative control), but present in cortex and tail tissue (http://www.informatics.jax.org/allele/MGI:2684610).

PCR-based genotyping assay was then performed by technical assistance. Several primer pairs (MWG – Ebersberg) were used for detecting Emx1 and NKCC1 gene: a primer pair binds to Emx1 DNA sequence (give a 400 bp gel band), a primer pair binds to $Emx1^{IREScre}$ DNA sequence (give an 120 bp gel band), a primer pair binds to NKCC1 and $NKCC1^{flox}$ DNA sequence (give a 220 bp gel band for NKCC1, and give a 320 bp gel band for $NKCC1^{flox}$), and a primer pair binds to recombined NKCC1 DNA sequence (give a 250 bp gel band). In NKCC1 KO^{Emx1} animals, homozygous recombined NKCC1 DNA sequence should be detected in cortex and tail tissue, but not in small intestine tissue (due to a lack of cre expression).

3.13 Chemicals

Chemicals were obtained from Sigma (bicuculline methiodide, bumetanide, isoguvacine, cadmium chloride), Tocris [DL-2-amino-5-phosphonopentanoic acid (APV), 6,7-dinitroquinoxaline-2,3(1H,4H)-dione (DNQX)], and Biotrend [tetrodotoxin (TTX)].

3.14 Data evaluation and statistics

Data were analyzed using pClamp 10, Microsoft Excel 2010, minianalysis 6.0, Stimfit, AutoSignal v1.7 and Matlab 2010a/2016a. Statistical analyses were performed using OriginPro 2018 and SPSS Statistics 22/24. Unless otherwise stated, the statistical parameter n refers to the number of animals in Ca^{2+} imaging experiments or to the number of cells in electrophysiological recordings. All data are reported as mean ± standard error of the mean (SEM). The Kolmogorov–Smirnov test or Shapiro–Wilk test was used to test for the normality of data. Parametric testing procedures were applied for normally distributed data; otherwise, non-parametric tests were used. In the case of two-sample t-tests and unequal group variances, Welch's correction was applied. P values (two-tailed tests) < 0.05 were considered statistically significant.

Chapter 4. Results

4.1 Part 1 [3]

Optogenetic tools for reversible silencing of neurons facilitate analyzing how distinct neuronal populations causally contribute to brain dynamics at the cellular, network and behavioral level. The light-driven Cl^- pump eNpHR3.0 is widely used as an inhibitory optogenetic tool. However, prominent inactivation appears during continuous illumination. Data obtained from structurally related opsins showed that short-wavelength visible light can accelerate recovery from inactivation. Here, it has been explored as to which extent this property could be exploited in order to increase the temporal stability of eNpHR3.0-mediated photo-currents.

4.1.1 Blue light accelerates the recovery of eNpHR3.0-mediated currents from inactivation in a duration- and power-dependent manner

To explore the potential benefits of alternative eNpHR3.0 photo-stimulation paradigms, an eNpHR3.0-EYFP fusion protein was expressed in cortical glutamatergic neurons using a transgenic approach (*Emx1^{IREScre}:eNpHR3.0-EYFP^{LSL}* mice) (Kummer et al. 2012). Whole-cell voltage-clamp recordings from identified $EYFP^+$ CA1 pyramidal cells were performed in the continuous presence of antagonists of voltage-gated Na^+ channels (0.5 µM TTX) and ionotropic glutamate and $GABA_A$ receptors (10 µM DNQX, 50 µM APV, 10 µM bicuculline) to abolish recurrent excitation and minimize synaptic noise. In agreement with published data (Alfonsa 2015, Zhang et al. 2007, Han and Boyden 2007), photo-stimulation using yellow light (594 nm, 5 mW at the tip of the optical fiber) induced outward currents that rapidly decayed to 34.2 ± 3.0% of the initial peak amplitude within ten seconds of continuous light exposure (I_{peak}: 62.0 ± 5.8 pA n = 15 cells; Fig. 2*A,B*). The recovery from inactivation by an additional 594-nm test pulse at variable time delays (Δt) was probed, and it was slow under control conditions (time constant of a mono-exponential fit, 54.1 ± 2.6 s, n = 7 cells; Fig. 2C).

[3] Results, text and figures of Part 1 have been modified and extended on the basis of a manuscript that is currently under preparation. For details regarding author contributions, please see "Ehrenwörtliche Erklärung".

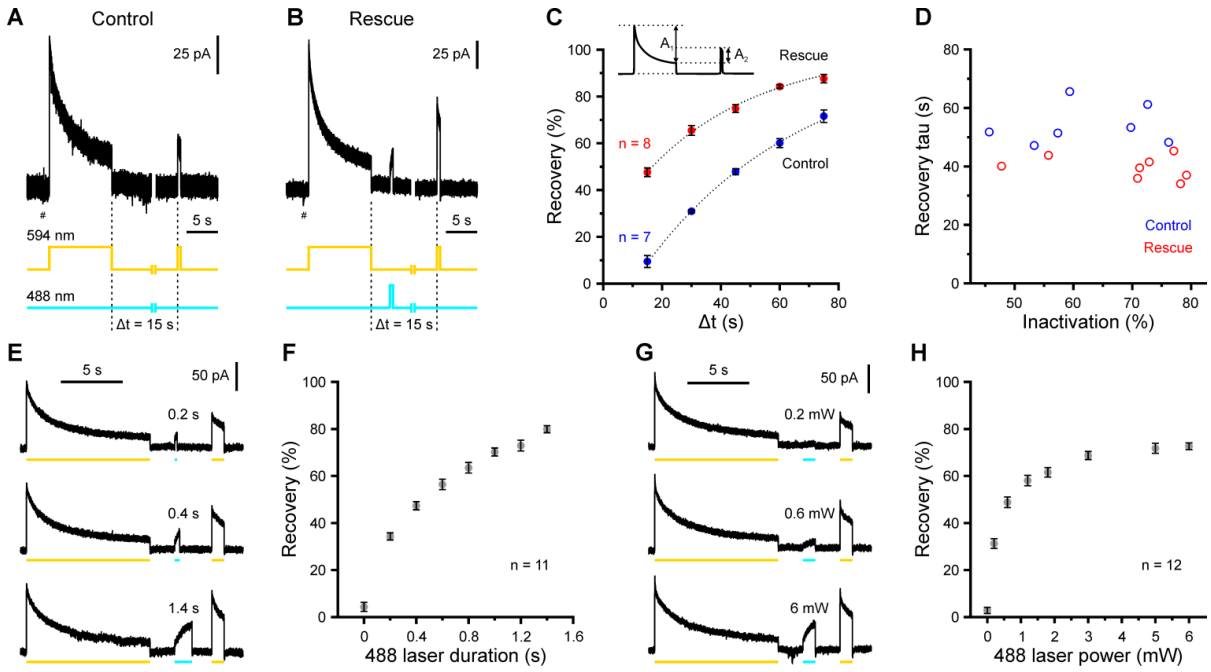

Figure 2. Blue light accelerates the recovery of eNpHR3.0-mediated currents from inactivation in a duration- and power-dependent manner. A, Sample voltage-clamp recording illustrating that prolonged (10 s) photo-stimulation at 594 nm (5 mW) induces pronounced inactivation of eNpHR3.0-mediated currents. Note that the recovery from inactivation is slow (test pulse at Δt = 15 s). B, Sample trace from another cell demonstrating that blue light (500 ms, 488 nm, 5 mW) accelerates the recovery from inactivation. Also note the outward current induced by blue light. C, Recovery of eNpHR3.0-mediated currents is enhanced by blue light. Inset, recovery is defined as the ratio of current amplitudes induced by the test (at Δt) versus initial pulse, measured relative to I_{late} (i.e. recovery = A_2/A_1). Dotted lines represent mono-exponential fits to population data. Each cell was tested for all values of Δt either without (Control, n = 7 cells) or with (Rescue, n = 8 cells) an intervening photo-stimulation at 488 nm (500 ms). In A and B, current responses to –10 mV voltage steps used to monitor access resistance are clipped for clarity (#). D, Independent of the degree of inactivation (1 - I_{late}/I_{peak}), time constants of recovery are lower for rescue as compared to control trials. Each symbol represents a single cell. E, Recovery from inactivation depends on the duration of the 488-nm rescue pulse (blue lines). All traces are from a single cell. F, Quantification. G, Recovery from inactivation depends on the power of the 488-nm rescue pulse. All traces are from a single cell. H, Quantification. Data are presented as mean ± SEM.

However, recovery from inactivation was significantly enhanced by a brief pulse of blue light (488 nm, 500 ms, 5 mW) [interaction (control/rescue × Δt): $F = 17.8$, $df = 4$, $P = 2.9 \times 10^{-9}$, n = 7/8 cells (control/rescue), mixed-model ANOVA; Δt = 15 s: $t(13) = -12.3$, $P = 1.5 \times 10^{-8}$, Δt = 30 s: $t(8.2) = 16.1$, $P = 1.6 \times 10^{-7}$, Δt = 45 s: $t(13) = -12.3$, $P = 1.6 \times 10^{-8}$, Δt = 60 s: $t(13) = 12.1$, $P = 1.9 \times 10^{-8}$, Δt = 75 s: $t(13) = -5.1$, $P = 2.1 \times 10^{-4}$, two-sample t-tests; Fig. 2*B,C*]. At the population level, the recovery time

constant was not significantly correlated to the degree of inactivation ($1 - I_{late}/I_{peak}$) induced by the initial photo-stimulation at 594 nm (Spearman's rank correlation coefficient = –0.38, P = 0.16, n = 15 cells; Fig. 2*D*). Next, the time and power dependent influences of blue-light rescue stimulation were addressed. In a first set of experiments, the duration of the 488-nm light pulse was systematically varied while keeping the applied power constant (5 mW). It was found that the recovery from inactivation monotonically increased with increasing duration of the blue-light pulse, showing no saturation even at the longest pulse duration (1.4 s) tested (F = 575, df = 3.2, P = 3.4×10^{-28}, n = 11 cells, one–way repeated–measures ANOVA, Huynh–Feldt correction; Fig. 2*E,F*). In a second set of experiments, the power of the 488-nm light pulse was systematically varied at a constant duration of 1 s. The recovery from inactivation significantly depended on the power of blue light (F = 529, df = 7, P = 2.3×10^{-62}, n = 12 cells, one–way repeated–measures ANOVA; Fig. 2*G,H*), but saturated at close to 3 mW.

Collectively, these data confirm and extend previous data demonstrating that blue light is suited to accelerate the recovery of eNpHR3.0-mediated currents from inactivation in a duration- and power-dependent manner.

4.1.2 Blue light attenuates the inactivation of eNpHR3.0-mediated currents during prolonged photo-stimulation in a mean power-dependent manner

Next, whether blue light may be similarly used to prevent the inactivation of eNpHR3.0-mediated currents when co-applied with photo-stimulation at 594 nm was assessed. To this end, cells were photo-stimulated with a constant power of 594-nm light (5 mW) and co-applied with a systematically varied power of 488-nm excitation (Fig. 3*A,B*). The effect was quantified by determining the remaining current at the end of photo-stimulation (I_{late}) as a fraction of the peak eNpHR3.0-mediated current (i.e. I_{late}/I_{peak}). It was found that the fraction of this non-inactivating current strongly depended on the power of blue light (F = 226, df = 3.7, P = 3.1×10^{-15}, n = 6 cells, one–way repeated–measures ANOVA, Huynh–Feldt correction; Fig. 3*B*). Due to the duration- and power-dependency of blue light on accelerating the recovery, therefore it was hypothesized that the mean power of blue light excitation determines the prevention of inactivation effect. To verify this, the effect of different stimulation regimes on prevention of inactivation was probed by keeping the delivered total

power of blue light constant. Pulsed stimulation, operating at a high-frequency (1 kHz) with a 20/80% (on/off) duty cycle, was achieved by means of an acousto-optic tunable filter (see Methods). In a first set of experiments, the effects of continuous *versus* pulsed photo-stimulation at a constant mean power of either 3 mW (Fig. 3*C*, *top*) or 0.2 mW was compared. This was achieved by compensatorily increasing the peak 488-nm light power in pulsed stimulation trials. At both power levels, non-inactivating current amplitudes did not significantly differ from those obtained during continuous stimulation (0.2 mW: 100.7 ± 2.1% of control, $t(4) = – 0.63$, $P = 0.56$, $n = 5$ cells, paired t-test; 3 mW: 102.6 ± 1.4% of control, $t(3) = – 1.98$, $P = 0.14$, $n = 4$ cells, paired t-test; Fig. 3*D, left*).

In an independent set of experiments, continuous and pulsed photo-stimulation were compared at a constant peak 488-nm light power of either 3 mW (Fig. 3*C*, *bottom*) or 0.2 mW, which effectively reduced the mean power in pulsed stimulation trials to 20%. In line with the above data, pulsed stimulation at constant peak power was significantly less effective in preventing inactivation as compared to continuous excitation, reflected in lower values of I_{late} (0.2 mW: 63.5 ± 4.0% of control, $t(4) = 7.11$, $P = 2.1 \times 10^{-3}$, $n = 5$ cells, paired t-test; 3 mW: 66.9 ± 5.7% of control, $t(3) = 7.14$, $P = 5.7 \times 10^{-3}$, $n = 4$ cells, paired t-test; Fig. 3*D, right*). Based on the same rationale and taking into consideration that the deactivation kinetics of eNpHR3.0-mediated currents is in the range of several milliseconds, next a potential benefit of pulsed [1 kHz, 20/80% (on/off) duty cycle] *versus* continuous photo-stimulation at 594 nm on the background of a continuous, constant-power (5 mW) excitation with blue light was investigated. It was found that I_{late} amplitudes did not significantly differ between the two regimes if the mean 594-nm light power was kept constant at 3 mW by compensatorily increasing the peak power in pulsed stimulation trials (normalized I_{late}: 96.0 ± 1.6%). In contrast, I_{late} was significantly reduced to 81.4 ± 1.1% if the peak 594-nm light power was unchanged (continuous/mean power = 3 mW vs. pulsed/mean power = 3 mW: $P = 0.21$, continuous/mean power = 3 mW vs. pulsed/mean power = 0.6 mW: $P = 7.4 \times 10^{-4}$, *post hoc* t-tests with Bonferroni correction; $F = 46.1$, $df = 2$, $P = 2.3 \times 10^{-6}$, $n = 7$ cells, one–way repeated–measures ANOVA).

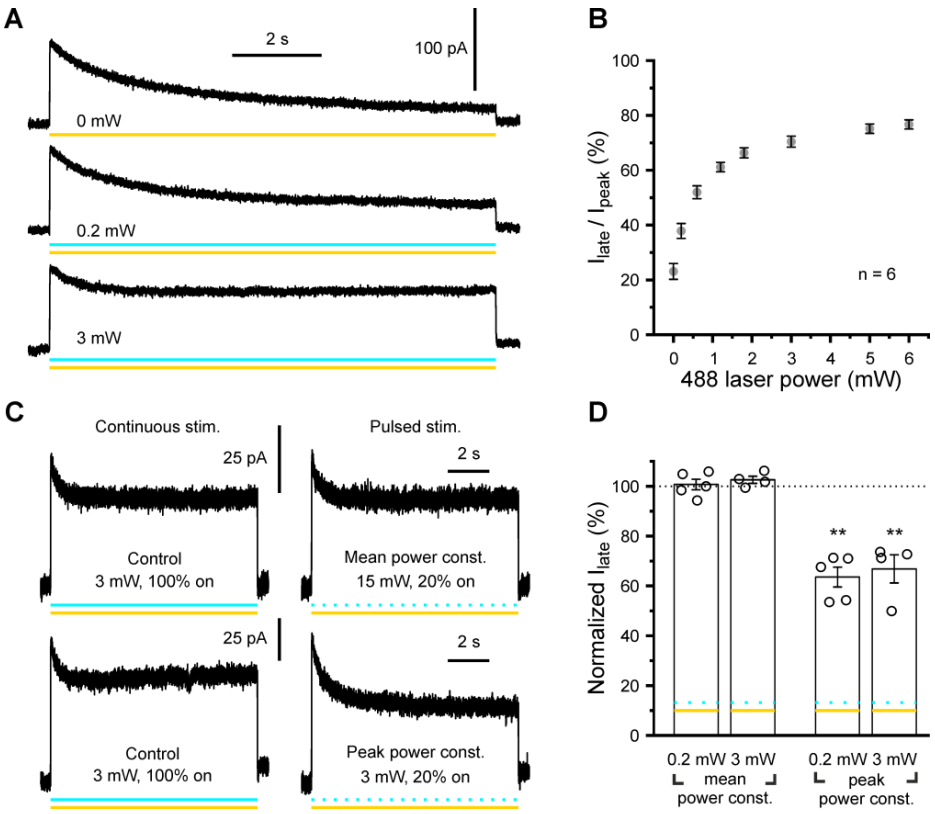

Figure 3. Co-stimulation at 594 nm and 488 nm attenuates the inactivation of eNpHR3.0-mediated currents during prolonged photo-stimulation in a mean power-dependent manner. A, Sample voltage-clamp recording from a single cell illustrating eNpHR3.0-mediated currents in response to photo-stimulation at 594 nm (5 mW) alone (top) or in combination with 488 nm at variable power levels (middle and bottom). Power levels indicated refer to 488-nm light. B, Dependence of inactivation on the power of 488-nm light. C, The rescue effect of 488-nm light on the inactivation of eNpHR3.0-dependent currents depends on its mean, rather than peak, power. Top, Continuous 488-nm-stimulation (left) is equally effective in attenuating inactivation as compared to pulsed (1 kHz, 20/80% on/off) stimulation at constant mean power (right). Bottom, Continuous 488-nm-stimulation (left) is more effective in attenuating inactivation as compared to pulsed (1 kHz, 20/80% on/off) stimulation at constant peak power (right). D, For quantification, Ilate measured during pulsed stimulation was normalized to Ilate obtained for the respective continuous-stimulation trials. Each symbol represents a single cell. Data are presented as mean ± SEM. ** $P < 0.01$.

In sum, present data demonstrate that blue light attenuates the inactivation of eNpHR3.0-mediated currents during prolonged photo-stimulation at 594 nm in a mean power-dependent manner. Analogously, the amplitude of the non-inactivating eNpHR3.0-dependent current is largely determined by the average, rather than the peak, 594-nm light power delivered.

4.1.3 Blue light alone enables efficient and stable long-term photo-stimulation of eNpHR3.0

While the previous experiments provide a strategy to enhance the temporal stability of eNpHR3.0-mediated currents, the initial data employing rescue pulses of blue light (Fig. 4*B*) already revealed that photo-stimulation at 488 nm alone is capable of inducing outwards currents in eNpHR3.0/-EYFP$^+$ cells, in line with previous reports (Han and Boyden 2007). Therefore experiments have been done to systematically investigate the properties of blue light-evoked photo-stimulation of eNpHR3.0.

To this end, cells were photo-stimulated at either 594 nm or 488 nm at power levels ranging from 1 to 5 mW (Fig. 4*A*). At each power level examined, I_{peak} values were significantly higher for yellow-light as compared to blue-light stimulation (1 mW: t(6) = –6.62, P = 5.7× 10^{-4}, 3 mW: t(6) = –7.35, P = 3.2 × 10^{-4}, 5 mW: t(6) = –6.57, P = 5.9 × 10^{-4}, n = 7 cells, paired t-tests; Fig. 4*A,C*) – in a power-dependent manner [interaction (594/488 nm × power): F = 24.9, df = 2, P = 5.4 × 10^{-5}, two-way repeated-measures ANOVA]. Strikingly, however, current responses evoked by blue-light photo-stimulation displayed an extraordinary temporal stability. This effect was quantified by determining the fraction of the non-inactivating current (i.e. I_{late}/I_{peak}; Fig. 4*D*), which was found to be considerably higher for photo-stimulation at 488 nm as compared to 594 nm (1 mW: t(6) = 11.94, P = 2.1 × 10^{-5}, 3 mW: t(6) = 19.69, P = 1.1 × 10^{-6}, 5 mW: t(6) = 30.21, P = 8.7 × 10^{-8}, n = 7 cells, paired t-tests; Fig. 4*A,D*). In addition, whereas the ratio I_{late}/I_{peak} strongly declined with increasing power levels for 594-nm light, this dependency was considerably weaker in case of photo-stimulation with blue light (Fig. 4*A,D*). As a result of this behavior, absolute non-inactivating current amplitudes (I_{late}) evoked at 594 nm *versus* 488 nm diverged in a power-dependent manner [interaction (594/488 nm × power): F = 42.3, df = 1.06, P = 4.6 × 10^{-4}, two-way repeated-measures ANOVA, Huynh–Feldt correction; Fig. 4*B*]. Next experiments were performed to determine as to which extent combinations of blue and yellow light, at constant total power (5 mW), could further increase I_{late}. Strikingly, all tested combinations of 488/594 nm as well as 488 nm alone clearly outperformed photo-stimulation with pure yellow light as reflected in higher values of I_{late} (594 nm *versus* all other groups: P = 5.1 × 10^{-3} or lower, *post hoc* t-tests with Bonferroni correction; F = 71.4, df = 1.3, P = 2.1 × 10^{-6}, n = 9 cells, one–way repeated–measures ANOVA, Huynh-Feldt correction; Fig. 4*E,F*). Highest values of I_{late} were

found for combinations with a blue light fraction of 40–60%, which moderately exceeded I_{late} values evoked by 488 nm alone (Fig. 4*F*).

Collectively, these data unexpectedly reveal that photo-stimulation at 488 nm either alone or combined with 594-nm light substantially enhances non-inactivating eNpHR3.0-mediated currents and profoundly improves their temporal stability.

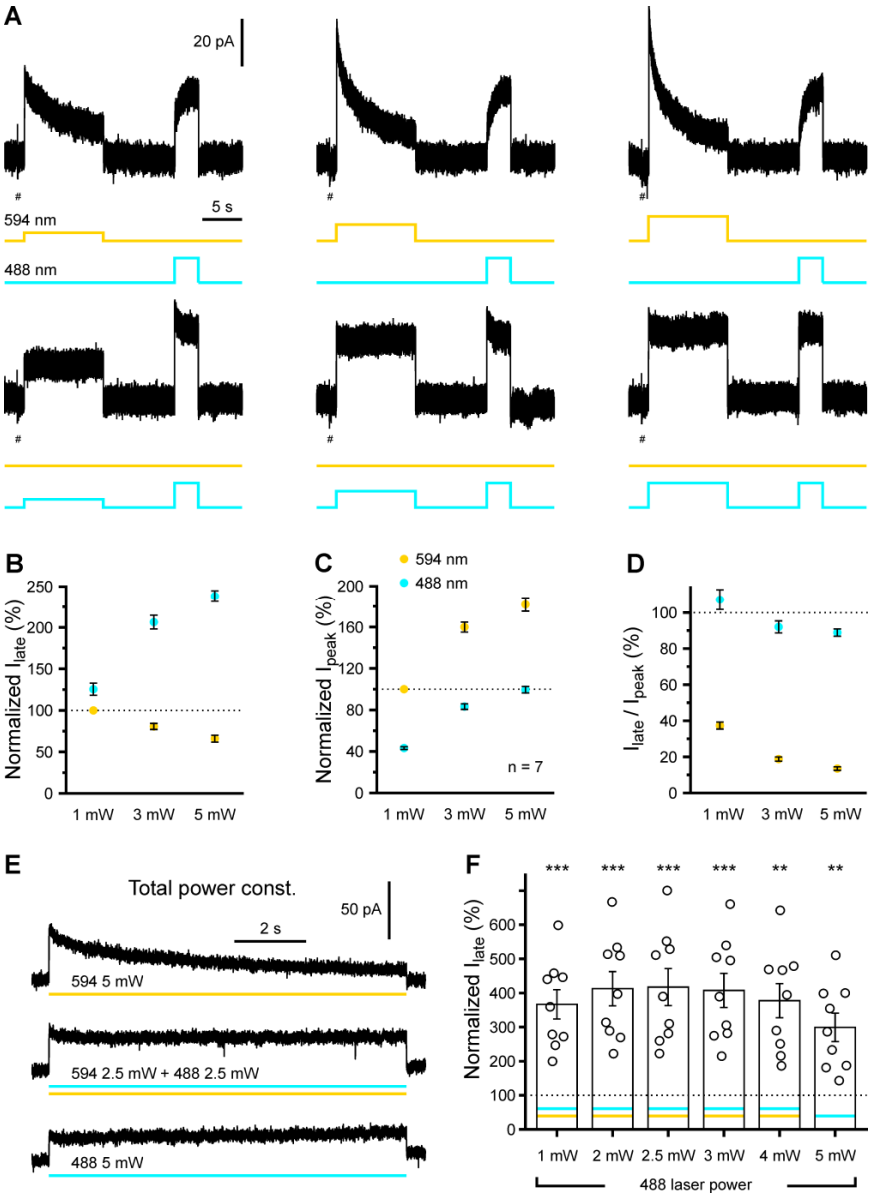

Figure 4. 488-nm light alone enables efficient and stable long-term photo-stimulation of eNpHR3.0. A, Sample voltage-clamp recordings from a single cell illustrating the power-dependence of HR-mediated currents evoked by photo-stimulation at 594 nm (top) or 488 nm (bottom), delivered at 1 mW (left), 3 mW (middle) or 5 mW (right). Note that photo-currents evoked at 488 nm display lower peak amplitudes, but high temporal stability across the entire power range examined. At the end of each trial, 488-nm light (5 mW) was used to accelerate the recovery from inactivation (note the difference in

onset kinetics of evoked currents depending on the degree of previous inactivation). Current responses to –10 mV voltage steps used to monitor access resistance are clipped for clarity (#). B–D, Late (I_{late}, B) and peak (I_{peak}, C) current amplitudes as well as the ratio of I_{late} versus I_{peak} (D) – normalized to the respective values at 594 nm and 1 mW (n = 7 cells). Note that E, Sample traces from a single cell photo-stimulated at 594 nm and/or 488 nm and a constant total light power of 5 mW. F, Quantification of I_{late} measured during the photo-stimulation regimes indicated normalized to I_{late} obtained by photo-stimulation at 594 nm (5 mW) alone. Note that each combination of 594 nm plus 488 nm tested (at constant total power) considerably outperformed photo-stimulation at 594 nm alone (dotted line). Each symbol represents a single cell. Data are presented as mean ± SEM. ** $P < 0.01$, *** $P < 0.001$.

4.1.4 Blue light-induced photo-stimulation of eNpHR3.0 enables efficient long-term hyperpolarization and inhibition

In a final step, whether the superior properties of blue-light photo-stimulation found in voltage-clamp experiments could translate into a higher efficiency of long-term neuronal inhibition was investigated. To this end, current-clamp measurements have been performed in the presence of ionotropic glutamate and GABA receptor antagonists in the absence of TTX and used repetitive 1-s current injections via the patch pipette in order to evoke AP firing (Fig. 5A). Photo-stimulation of eNpHR3.0 at 594 nm (5 mW) for 1 min suppressed AP discharge in a highly time-dependent manner: Whereas firing in response to the first test pulse (500 ms after the onset of light stimulation) was virtually abolished, the inhibitory effect almost disappeared for the second as well as all subsequent test pulses (Fig. 5*A,B*).

In contrast, photo-stimulation at 488 nm (5 mW) reliably inhibited AP discharge during the entire 1-min-period of light exposure [interaction (Control/488 nm/594 nm × test pulse number): $F = 13.2$, $df = 4.6$, $P = 1.7 \times 10^{-7}$, n = 10 cells, two–way repeated–measures ANOVA, Huynh–Feldt correction; Fig. 5*A,B*]. Furthermore, photo-stimulation with yellow light resulted in a pronounced, but transient hyperpolarization, whereas photo-stimulation at 488 nm induced a highly stable hyperpolarizing response in all cells analyzed. Accordingly, a two-way repeated-measures ANOVA yielded a highly significant interaction between the independent variables ($F = 71.2$, $df = 5.0$, $P = 3.1 \times 10^{-20}$, n = 10 cells, Huynh–Feldt correction; Fig. 5*A,C*).

In conclusion, photo-stimulation with blue light renders eNpHR3.0 suitable for long-term neuronal hyperpolarization and inhibition.

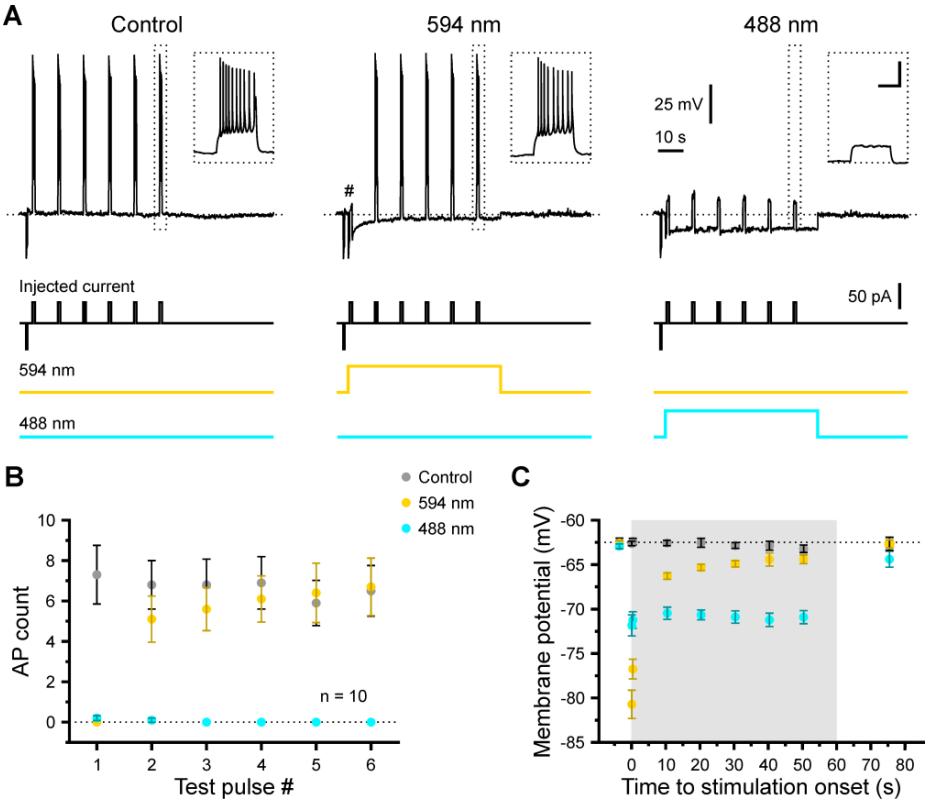

Figure 5. Photo-stimulation of eNpHR3.0 at 488 nm enables efficient long-term hyperpolarization and inhibition. A, Sample current-clamp measurements from a single cell (biased to about -65 mV at rest) repetitively challenged with an inward current of constant amplitude either without (5 mW, left) or with photo-stimulation at 594 nm (5 mW, middle) or 488 nm (right), respectively. Note that yellow-light stimulation initially abolished AP firing (#), which recovered during prolonged photo-stimulation periods. Also note that blue-light stimulation suppressed firing for the entire 1-min period on the background of a stable hyperpolarization. Insets, current responses to the last test pulse at higher temporal magnification (scale bars, 25 mV, 0.5 s). B, Number of APs as a function of the test pulse-number. C, Time-course of membrane potential (grey – period of photo-stimulation). Data are presented as mean ± SEM.

4.2 Part 2

The depolarizing mode of GABAergic transmission was thought to contribute to the generation of spontaneous correlated network activity and affect the maturation of the cortical network by promoting synaptogenesis. The present work examined the role of depolarizing GABA in Emx1 positive cells for cortical network development.

4.2.1 Activation of eNpHR3.0 in Emx1^{IREScre} positive cells rescues bumetanide sensitive GDPs in hippocampus *in vitro*

Ample data showed that the NKCC1 antagonist bumetanide blocks spontaneous correlated network activity in the neonatal hippocampus *in vitro*, and this blocking effect was attributed to breakdown of $[Cl^-]_{in}$ (Kirmse et al. 2015, Wang and Kriegstein 2011, Kirmse et al. 2010, Nardou et al. 2009, Zhu et al. 2008, Wang and Kriegstein 2008, Tyzio et al. 2008, Owens et al. 1996). It is unclear whether loading Cl^- in a cell-type specific manner would restore spontaneous correlated network activity blocked by bumetanide application. Therefore by making novel use of the Cl^- pumping property of eNpHR3.0, experiments were carried out to explore whether activation of eNpHR3.0 in Emx1 positive cells might rescue spontaneous correlated network activity blocked by bumetanide application. To do this, whole-cell patch-clamp recordings were performed from CA3 pyramidal cells of *Emx1^{IREScre}:eNpHR3.0-EYFP^{LSL}* mice at the age of P3-6 *in vitro.* Bursts of spontaneous postsynaptic current (sPSCs) (see Methods), which reflect correlated network activity, were counted for the whole recording duration with a bin-size of 20 seconds. In line with published data, here, after 10 min of bumetanide (10 µM) perfusion sPSC bursts were reduced in frequency (Fig. 6A, middle). Under bumetanide perfusion, continuous 488 nm laser stimulation (5 mW for 60 seconds) transiently increased the mean burst count per bin as compared to before the light stimulus [before stimulus: 0.35 ± 0.19 per bin, n = 4 cells, after stimulus: 4.25 ± 0.66 per bin, n = 4 cells, t = –6.57, P = 7.2×10^{-3}, paired t-test, Fig. 6C].

These data suggest that activation of eNpHR3.0 in Emx1^{IREScre} positive cells is sufficient to rescue bumetanide sensitive sPSC bursts, which indicates that depolarizing GABA in Emx1 positive pyramidal cells importantly contributes to the generation of spontaneous network activity in the hippocampus *in vitro*.

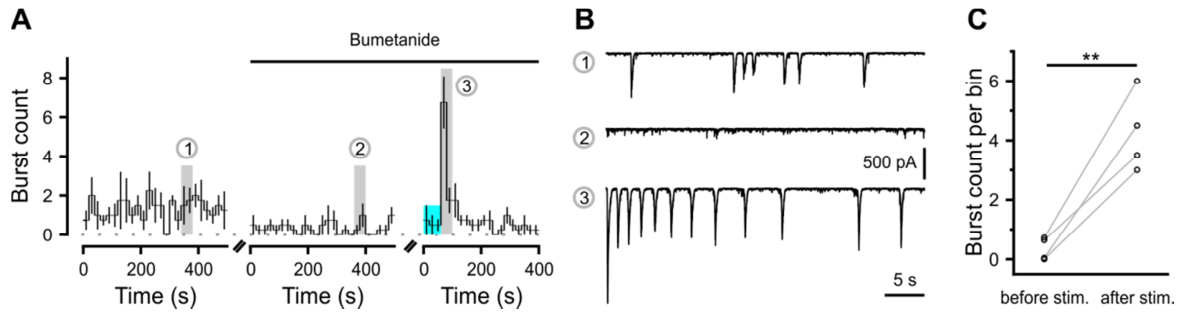

Figure 6. Emx1^{IREScre} dependent optogenetic stimulus rescues bumetanide sensitive spontaneous postsynaptic burst. A, Time course of visually detected spontaneous burst count (binsize of 20 seconds). Whole cell voltage clamp recordings were performed from CA3 pyramidal cells of acute hippocampus slices. Each recorded cell had three recording time periods, the first break of recording time line represents already under continuously bumetanide (50 µM) perfusion for at least 10 min to allow achieve of steady state block of NKCC1 function. After the second break of recording time line, 488 nm laser (5 mW) was continuously applied for 60 seconds, cyan color labeled region. B, Sample recordings. C, Statistics of the mean burst count per bin. Data are presented as mean ± SEM, ** P < 0.01.

4.2.2 NKCC1 contributes to GABAergic depolarization and $GABA_AR$-mediated excitation *in vitro* [4]

Since these results with pharmacological approach point to an important role of $[Cl^-]_{in}$ and GABA-mediated depolarization in pyramidal cells, further experiments using a genetic approach were performed to explore the contribution of NKCC1 in Emx1 positive cells to the generation of spontaneous network activity. As a first step, the role of NKCC1 in maintaining the depolarizing effect of GABA *in vitro* was examined. To this end, cell-type specific disruption of NKCC1 was achieved by crossing floxed NKCC1 mice to the Emx1^{IREScre} knockin mice. To noninvasively assess the effect of GABA on membrane potential, gramicidin-perforated current-clamp recordings at zero transmembrane currents (Fig. 7A) were applied (Zhu et al. 2008). To abolish recurrent excitation and to minimize synaptic noise, the recordings were performed in the continuous presence of antagonists of voltage-gated Na^+ channels (0.5 µM TTX) and ionotropic glutamate receptors (10 µM DNQX, 50 µM APV), moreover 100 µM

[4] Results, text and figures related to paragraphs 4.2.2 – 4.2.6 and 4.2.8 – 4.2.9 have been modified and extended on the basis of a manuscript that is currently under preparation. For details regarding author contributions, please see "Ehrenwörtliche Erklärung".

$CdCl_2$ was added to avoid an amplification of depolarization by voltage-gated calcium channels. Recordings were performed from CA3 pyramidal cells in acute horizontal brain slices of both NKCC1 WT and NKCC1 KO^{Emx1} animals at the age of P3-4. The measured resting membrane potential (V_{rest}) was not significantly different between cells from NKCC1 WT and NKCC1 KO^{Emx1} animals (WT: –73.0 ± 0.6 mV, n = 15, KO: –73.3 ± 0.9 mV, n = 10, P = 0.78; Mann–Whitney U test; Fig. 7C). Further, puff applied isoguvacine (10 psi, 2 seconds, 100 µM) induced depolarization in cells from both NKCC1 WT and NKCC1 KO^{Emx1} animals (Fig. 7B). However, cells from NKCC1 KO^{Emx1} animals showed significantly lower peak isoguvacine induced membrane potential (V_{peak}) compared with those obtained from WT animals (WT: –50.9 ± 1.9 mV, n =15, KO^{Emx1}: –58.6 ± 2.8 mV, n = 10, P = 0.028, two-sample t-test). Moreover, isoguvacine-induced membrane potential changes (ΔV_m) in two subsequent trials were highly correlated (WT: Spearman's rho = 0.775, P = 6.9×10^{-4}, KO^{Emx1}: Spearman's rho = 0.733, P = 0.016 Fig. 7D), while NKCC1 KO^{Emx1} animals showed significantly reduced ΔV_m compared with WT animals ($\Delta V_{m,\ trial1}$ WT: –22.1 ± 1.9 mV, n = 15, KO^{Emx1}: –14.7 ± 2.4 mV, n = 10, P = 0.023, two-sample t-test; $\Delta V_{m,\ trial2}$ WT: –19.3 ± 1.8 mV, n = 15, KO^{Emx1}: –12.3 ± 1.7 mV, n = 10, P = 0.013, two-sample t-test). Thus, $Emx1^{IREScre}$ dependent NKCC1 disruption attenuates isoguvacine-induced depolarization in hippocampal CA3 pyramidal cells.

It has been shown that depolarizing GABA could trigger AP firing in neonatal neurons *in vitro* (Tyzio et al. 2011, Kirmse et al. 2010). Next whether reduced isoguvacine-induced depolarization by $Emx1^{IREScre}$ dependent NKCC1 disruption result in a difference of isoguvacine-induced AP firing between CA3 pyramidal cells from NKCC1 WT and NKCC1 KO^{Emx1} animals at this age was explored. For this purpose, tight-seal cell-attached voltage-clamp recordings were applied. The command potential was manually adjusted to keep the amplifier baseline current at zero during recording, in order not to affect the cell membrane potential by the recording itself (Perkins 2006).

Recordings were performed in the continuous presence of ionotropic glutamate receptors antagonists (10 µM DNQX, 50 µM APV) to abolish recurrent excitation. For statistics, action current counts 300 ms before and after isoguvacine puff (100 ms, 10 psi, 100 µM) onset were analyzed. In cells from NKCC1 WT animals, mean action current count was significantly increased after isoguvacine puff application (P = 2.6×10^{-4}, n = 22, paired t-test), while no significant change was observed for cells from

NKCC1 KO^{Emx1} animals (P = 0.57, n = 16, Wilcoxon signed-rank tests). For statistical comparison, cells with an AP count increase were operationally defined as responsive. With this definition, the fraction of responsive cell was significantly lower for cells from KO^{Emx1} animals (3 out of 16 cells) compared to that from WT animals (17 out of 22 cells) (P = 3.6 × 10^{-4}, n = 38, chi-squared test, Fig. 7G, trial 1). In the subsequent trial, the fraction of responsive cells was also significantly lower for cells from KO^{Emx1} animals (1 out of 16 cells) compared to that from WT animals (15 out of 22 cells) (P = 1.3 × 10^{-4}, n = 38, chi-squared tests).

In summary, Emx1^{IREScre} dependent NKCC1 disruption attenuates GABAergic depolarization and further leads to reduced $GABA_AR$-mediated AP firing in CA3 pyramidal cells *in vitro*.

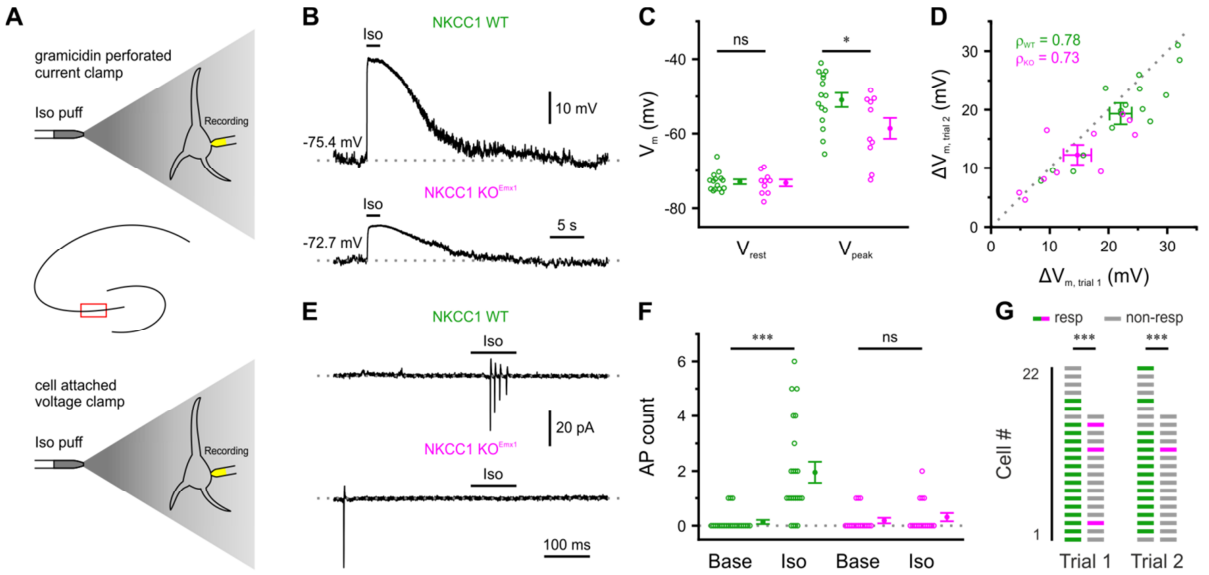

Figure 7. Conditional NKCC1 deletion attenuates GABAergic depolarization. A, Schematic drawing of experiment methods. Recordings were performed from CA3 pyramidal cells of acute hippocampus slices. Area marked with red rectangle. B, Sample gramicidin perforated-patch current-clamp recordings in response to puff-application of isoguvacine (Iso). C, Quantification of resting (V_{rest}) and peak isoguvacine-induced (V_{peak}) membrane potentials. D, High correlation of isoguvacine-induced membrane potential changes (ΔV_m) in two subsequent trials. ρ denotes the Spearman's rank correlation coefficient. E, Sample cell-attached recordings in response to puff-application of isoguvacine. F, Number of action currents detected in 300-ms intervals immediately before (Base) and after (Iso) puff onset. G, The fraction of responsive cells (resp) was significantly lower for cells from KO^{Emx1} vs. WT mice. Data are presented as mean ± SEM. ns – not significant, * P < 0.05, *** P < 0.001.

4.2.3 Emx1^{IREScre} dependent NKCC1 deletion impairs the generation of correlated hippocampal network activity *in vitro*

Next, the influence of NKCC1 disruption on the generation of spontaneously correlated network activity during the first postnatal week in the hippocampus was explored. To do this, sGPSCs were recorded in the absence of synaptic blockers via whole-cell patch-clamp from CA3 pyramidal cells of both NKCC1 WT and NKCC1 KO^{Emx1} animals at the age of P1-3 *in vitro*. Template matching was applied for the detection of sGPSCs. The mean sGPSC frequency was not significantly different between cells from NKCC1 WT and NKCC1 KO^{Emx1} animals (WT: 1.98 ± 0.83 Hz, n = 7; KO^{Emx1}: 4.40 ± 1.28 Hz, n = 13; P = 0.20, Mann-Whitney U-test, Fig. 8B). However, visually, recordings from NKCC1 WT animals showed more synchronized sGPSC bursts compared to that of NKCC1 KO^{Emx1} animals (Fig. 8A). To quantify this, the fraction of inter-sGPSC intervals ≤ 50 ms for each recorded cell was computed and defined this measure as burst index. Since with increasing sGPSC frequency, inter-event intervals will decrease, burst index as a parameter is highly dependent on sGPSC frequency. To help the interpretation of calculated burst indices from recordings, analytical burst index at different sGPSC frequency were calculated based on Poisson distribution (details see Methods) (Fig. 8C dotted line). Burst indices derived from NKCC1 WT animals were deviating more from the expected value of individual simulated burst index value as compared to that of NKCC1 KO^{Emx1} animals (Fig. 8C), which suggests that sGPSCs from NKCC1 WT do not occur stochastically. In contrast, burst indices derived from NKCC1 KO^{Emx1} animals were in a large portion overlapping with the simulated values, indicating a random occurrence of sGPSCs. Further, since the mean sGPSC frequency did not differ between NKCC1 WT and NKCC1 KO^{Emx1}, burst indices therefore were directly compared. Burst index from NKCC1 WT animals was significantly larger than that of NKCC1 KO^{Emx1} animals (WT: 0.34 ± 0.04, n = 6 cells [one cell excluded for calculation due to a low sGPSC number]; KO^{Emx1}: 0.20 ± 0.04, n = 13 cells, P = 0.016, Mann-Whitney U-test, Fig. 8D).

These data suggest that Emx1^{IREScre} dependent NKCC1 disruption impairs the generation of correlated hippocampal network activity *in vitro*.

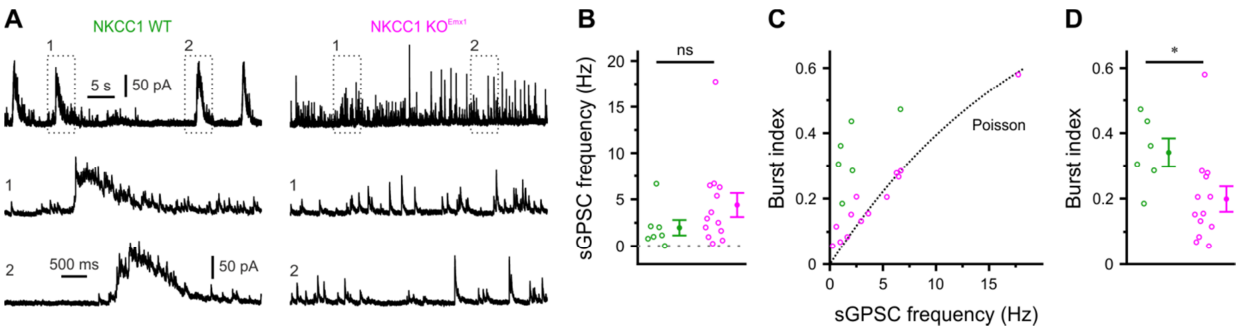

Figure 8. Conditional NKCC1 deletion impairs the generation of correlated hippocampal network activity. A, Sample whole-cell recordings of spontaneous GABAergic postsynaptic currents (sGPSCs) isolated by their reversal potential. B, Quantification of sGPSC frequency. C, Burst index as a function of sGPSC frequency. The dotted line represents the expected value for stochastic event trains obeying a Poisson point process. D, Quantification of burst indices. Data are presented as mean ± SEM. ns – not significant, * P < 0.05.

4.2.4 Intrinsic excitability and passive properties are unaltered in NKCC1 KO^{Emx1} mice *in vitro*

The impaired ability to generate correlated network activity might be due to a change of intrinsic excitability in the absence of functional NKCC1. To explore this possibility, spontaneous AP firing as an overall readout of intrinsic excitability was recorded. Non-invasive cell-attached voltage-clamp recordings were performed from CA3 pyramidal cells of both GCaMP3 NKCC1 WT and GCaMP3 NKCC1 KO^{Emx1} animals (Fig. 9A). Recordings were performed in the continuous presence of antagonists of ionotropic glutamate receptors and $GABA_A$ receptors (10 µM DNQX, 50 µM APV, 10 µM bicuculline) to abolish network inputs. The mean spontaneous AP (sAP) frequency did not differ between GCaMP3 NKCC1 WT and GCaMP3 NKCC1 KO^{Emx1} animals (WT: 0.315 ± 0.088 Hz, n=8 cells, KO^{Emx1}: 0.286 ± 0.113 Hz, n=11 cells, P = 0.39, Mann-Whitney test, Fig. 9B). Further experiments have been done to explore passive properties and active properties of pyramidal cells. For this, whole-cell recordings were performed using a K-gluconate based intra-pipette solution. Passive properties, which were extracted from the passive response induced by a –10 mV voltage step under voltage-clamp, including membrane capacitance (C_m), membrane input resistance (R_{input}) and membrane tau (τ_m), were all not significantly different between cells from GCaMP3 NKCC1 WT and GCaMP3 NKCC1 KO^{Emx1} animals [C_m (WT: 45.3 ± 3.3 pF, n = 19, KO^{Emx1}: 55.2 ± 5.2 pF, n = 16, P = 0.12, Mann-Whitney

test, Fig. 9C), R_{input} (WT: 0.733 ± 0.067 GΩ, n = 19, KO^{Emx1}: 0.681 ± 0.075 GΩ, n = 16, P = 0.61, two sample t-test, Fig. 9D), τ_m (WT: 33.8 ± 4.4 ms, n = 19, KO^{Emx1}: 35.5 ± 3.7 ms, n = 16, P = 0.78, two sample t-test, Fig. 9E)].

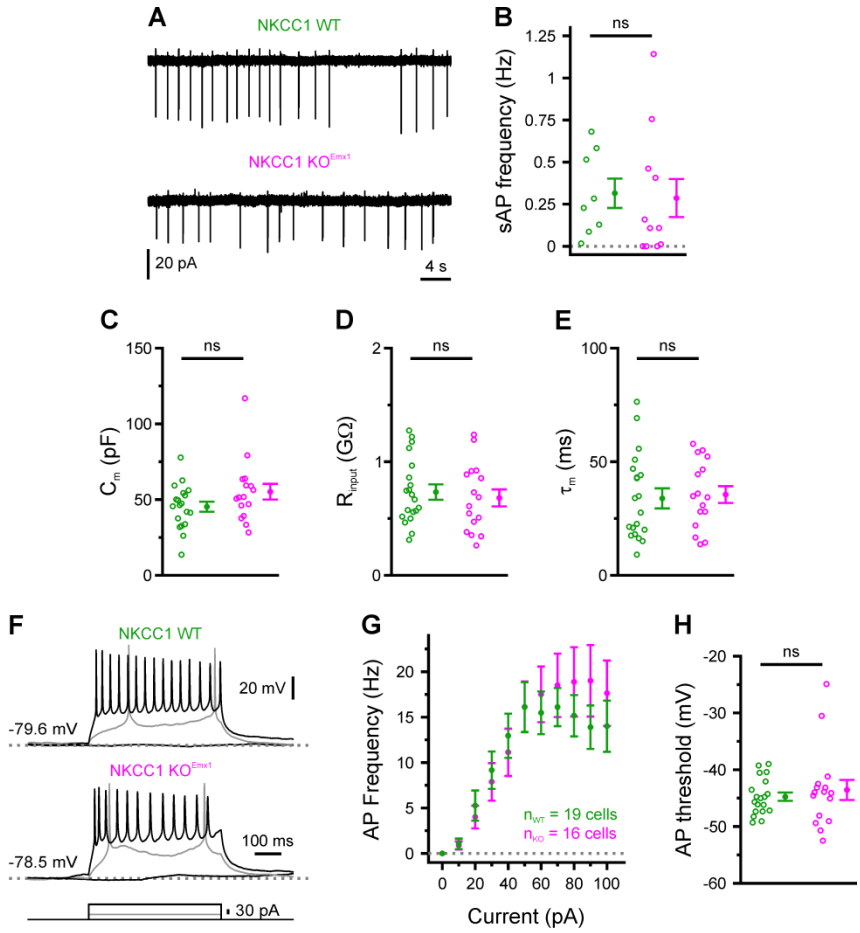

Figure 9. NKCC1 $Emx1^{IREScre}$ dependent disruption does not alter intrinsic excitability and passive properties. A, Sample cell-attached recordings of spontaneous action potential (AP) firing in the presence of ionotropic glutamate and GABA receptor antagonists. B, Mean spontaneous AP frequency. C, Membrane capacitance (C_m). D, Membrane input resistance (R_{input}). E, Membrane constant (τ_m). F, Sample whole-cell current-clamp recordings in response to current injections. G–H, Current-frequency relationship (G) and AP threshold (H) are unaffected in KO^{Emx1} mice. Data are presented as mean ± SEM. ns – not significant.

For active properties, series steps of current injections were applied (Fig. 9F, details see Methods). With increasing current injection, mean AP frequency was increased for recordings from both GCaMP3 NKCC1 WT and GCaMP3 NKCC1 KO^{Emx1} animals (injection current, WT: 19 cells, KO^{Emx1}: 16 cells, F = 32.9, df = 2.59, P = 4.0×10^{-13}, mixed model ANOVA, Huynh-Feldt correction). However, mixed model ANOVA

showed no significant interaction between injection current and genotype [interaction: (injection current × genotype): F = 1.01, df = 2.59, P = 0.30, Huynh-Feldt correction] and also no main effect of genotype (WT: 19 cells, KO^{Emx1}: 16 cells, F = 0.184, df = 1, P = 0.67, Fig. 9G). Moreover, AP threshold extracted at the 10 mV/ms rising slope from the first AP induced by current injection, was also not significantly different between cells from GCaMP3 NKCC1 WT and GCaMP3 NKCC1 KO^{Emx1} animals (WT: –44.8 ± 0.7 mV, n = 19 cells, KO^{Emx1}: –43.6 ± 1.8 mV, n = 16 cells, P = 0.80, Mann-Whitney test, Fig. 9H).

In summary, $Emx1^{IREScre}$ dependent NKCC1 disruption does not alter intrinsic excitability, including passive properties and active properties.

4.2.5 Maturation of basic synaptic properties is unaffected by $Emx1^{IREScre}$ dependent NKCC1 disruption

NKCC1 disruption might affect the maturation of synaptic properties and, in turn, lead to impaired correlated hippocampal network activity *in vitro*. To explore this possibility, miniature postsynaptic currents were recorded from CA3 pyramidal cells in both NKCC1 WT and NKCC1 KO^{Emx1} animals at P3–4 and P14-16. During this period, CA3 neurons undergo intense synaptogenesis and re-organization in subunit composition of both $GABA_A$Rs and AMPARs (Wang et al. 2014, Stubblefield and Benke 2010, Micheva and Beaulieu 1996).

Miniature AMPAR-mediated postsynaptic currents (mEPSCs) were recorded in the continuous presence of antagonists of voltage-gated Na^+ channels (0.5 µM TTX), NMDAR (50 µM APV) and $GABA_A$R (10 µM bicuculline). The mean mEPSC frequency developmentally increased for cells from both NKCC1 WT and NKCC1 KO^{Emx1} animals (Fig. 10A). However, no significant difference between genotypes was found [interaction age × genotype: P = 0.69, main effect of age: P = 9.6×10^{-4}, main effect of genotype: P = 0.73, two way ANOVA, Fig. 10C left]. In addition, median mEPSC amplitude as a measure of quantal size was developmentally increased for cells from both genotypes, but not significantly differ between genotypes [mEPSC amplitude: (interaction age × genotype): P = 0.95, main effect of age: P = 4.3×10^{-3}, main effect of genotype: P = 0.35, two way ANOVA, Fig. 10C middle]. The mean mEPSC decay time constant, which reflects subunit composition, was developmentally increased for cells from both genotypes, but also not

significantly different between genotypes [mEPSC decay: (interaction age × genotype): P = 0.63, main effect of age: P = 4.8 × 10^{-8}, main effect of genotype: P = 0.34, two way ANOVA, Fig. 10C right].

Miniature GABAergic postsynaptic currents (mGPSCs) were recorded in the continuous presence of antagonists of voltage-gated Na^+ channels (0.5 µM TTX), NMDAR (50 µM APV) and AMPAR (10 µM DNQX). Mean mGPSC frequency developmentally increased for cells from both NKCC1 WT and NKCC1 KO^{Emx1} animals (Fig. 10B), however no significant difference between genotypes was found (interaction age × genotype: P = 0.26, main effect of age: P = 1.2 × 10^{-27}, main effect of genotype: P = 0.56, two way ANOVA, Fig. 10D left). The median amplitude of mGPSC remained unchanged during development for cells from both genotypes [(interaction age × genotype): P = 0.083, main effect of age: P = 0.14, main effect of genotype: P = 0.82, two way ANOVA, Fig. 10D middle]. In addition, mGPSC decay time constant developmentally decreased for cells from both genotypes, but not significantly different between genotypes [(interaction age × genotype): P = 0.073, main effect of age: P = 4.3 × 10^{-17}, main effect of genotype: P = 0.68, two way ANOVA, Fig. 10D right].

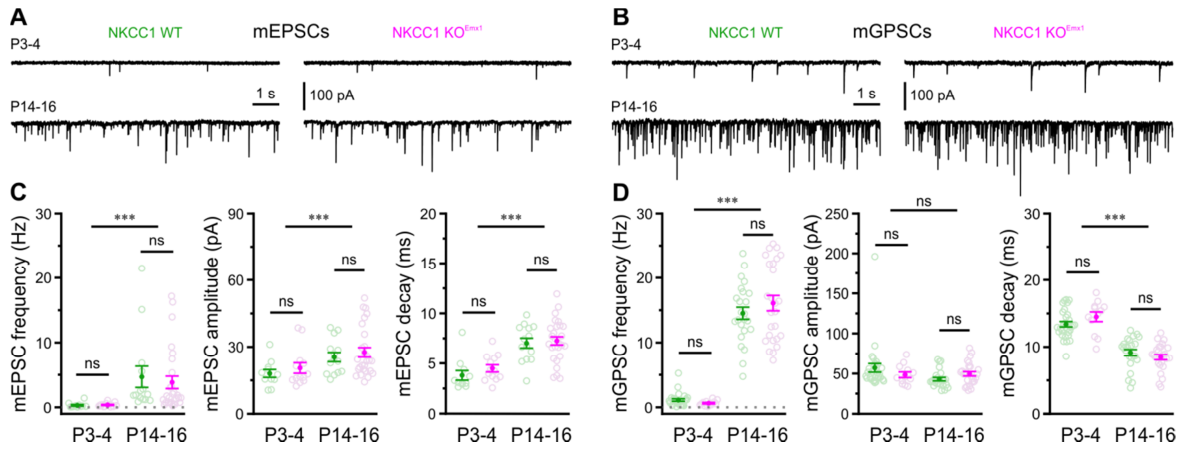

Figure 10. Maturation of basic synaptic properties is not affected by NKCC1 $Emx1^{IREScre}$ dependent disruption. A, Sample voltage-clamp measurements demonstrating AMPAR-dependent glutamatergic mEPSCs at P3–4 and P14–16. C, Mean mEPSC frequency (left), median mEPSC amplitude (middle) and mean mEPSC decay time constant. B, Sample voltage-clamp measurements demonstrating GABAergic mGPSCs at P3–4 and P14–16. D, Mean mGPSC frequency (left), median mGPSC amplitude (middle) and mean mGPSC decay time constant. Data are presented as mean ± SEM. ns – not significant, *** P < 0.001.

In summary, the maturation of basic synaptic properties is not affected by the conditional disruption of NKCC1 and is unlikely to account for the dramatic alteration of CA3 network activity induced by loss of NKCC1.

4.2.6 $Emx1^{IREScre}$ dependent NKCC1 deletion attenuates $GABA_AR$-mediated action potential firing in visual cortex

Although a strong influence of depolarizing GABA on network activity in the hippocampus *in vitro* was observed, it is still unclear whether or not this is a general phenomenon during neuronal network development. To address this question, next experiments were performed for elucidating how depolarizing GABA contributes to the generation of network activity in visual cortex *in vivo*. As a first step, whether in visual cortex GABAergic excitation was similarly affected by NKCC1 disruption was investigated. To do this, non-invasive tight-seal cell-attached voltage-clamp recordings from layer 2/3 visual cortex pyramidal cells in coronal slices were performed to compare $GABA_AR$ agonist-induced AP firing. Recordings were performed in the continuous presence of ionotropic glutamate receptors antagonists (10 µM DNQX, 50 µM APV) to abolish recurrent excitation. For statistics, action current counts 300 ms before and after isoguvacine puff onset were analyzed. In cells from GCaMP3 NKCC1 WT animals, mean action current count was significantly increased after isoguvacine puff application ($P = 0.042$, $n = 22$, Wilcoxon signed-rank tests), while no significant change was observed for cells from GCaMP3 NKCC1 KO^{Emx1} animals ($P = 0.35$, $n = 18$, Wilcoxon signed-rank tests). Further, the fraction of responsive cells was significantly lower for NKCC1 KO^{Emx1} animals (2 out of 18 cells) compared to NKCC1 WT (10 out of 22 cells) animals ($P = 0.018$, $n = 40$, chi-squared tests, Fig. 11C, trial 1). Two additional trials were recorded at intervals of 1 min (Fig. 11C), and for both trials statistics also revealed a significantly lower fraction of responsive cells for NKCC1 KO^{Emx1} animals compared to NKCC1 WT animals [trial 2: WT (12 out of 22 cells), KO^{Emx1} (3 out of 18 cells), $P = 0.014$, $n = 40$, chi-squared tests, trail 3: WT (12 out of 22 cells), KO^{Emx1} (3 out of 18 cells), $P = 0.014$, $n = 40$, chi-squared tests, Fig. 11C].

In conclusion, conditional NKCC1 deletion attenuates or abolishes $GABA_AR$ mediated AP firing in visual cortex.

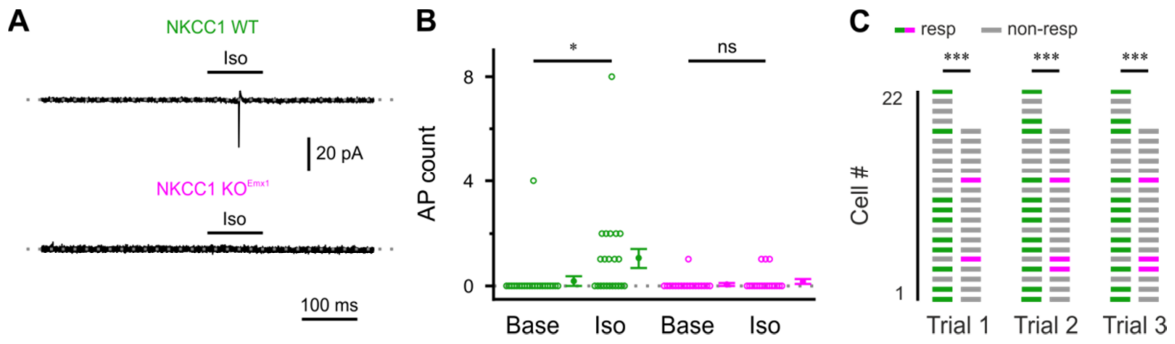

Figure 11. Conditional NKCC1 deletion attenuates $GABA_A$ receptor mediated AP firing in visual cortex. A, Sample cell-attached recordings in response to puff-application of isoguvacine, recordings were performed from layer 2/3 visual cortex pyramidal cells in coronal slices. B, Number of action currents detected in 300-ms intervals immediately before (Base) and after (Iso) puff onset. G, The fraction of responsive cells (resp) was significantly lower for cells from KO^{Emx1} vs. WT mice. Data are presented as mean ± SEM. ns – not significant, * $P < 0.05$, *** $P < 0.001$.

4.2.7 Characterization of spontaneous activity in neonatal visual cortex *in vivo*[5]

Electrophysiological recordings have shown that spontaneous network activity in the neonatal visual cortex is highly spatiotemporally synchronized, and sensory input independent spontaneous retinal waves largely contribute to the generation of them (Hanganu et al. 2007, Hanganu et al. 2006). In order to non-invasively characterize spontaneous cortical network activity with high spatial resolution, 3D voxel-based two-photon Ca^{2+} imaging paired with wide-band (0-6000 Hz) extracellular recordings were performed in N_2O anesthetized $Emx1^{IREScre}$:$GCaMP3^{LSL}$ mice at the age of P3-4. Voxel imaging was based on a spiral scanning of a cylindrical volume with a radius of 250 µm and a height of 200 µm, covering part of visual cortex. The scanning frequency was 10 Hz. For analysis, the cylindrical volume was subdivided into regular cubic voxels (side length, 25 µm) (Fig. 12A, left). Fluorescence time courses were extracted in each voxel and Ca^{2+} transients were detected with an unbiased template matching algorithm. It was found that spontaneous visual cortex activity was typically highly spatiotemporally synchronized, that is, large numbers of neighboring voxels co-activate close in time (Fig. 12A, right). A temporal criterion was applied to define Ca^{2+} clusters, neighboring transients were considered to belong to a common cluster

[5] Results, text and figures related to paragraph 4.2.7 have been modified from a published manuscript (Kummer et al. 2016). For details regarding author contributions, please see "Ehrenwörtliche Erklärung".

if they were separated by ≤500 ms. The spatial distribution of active and inactive voxels within Ca^{2+} clusters appeared to be highly non-stochastic as revealed by their reconstruction in 3D space (Fig. 12B, top row), which showed a prominent spatial confinement in the horizontal (x–y) plane and involved voxels along the entire depth (z) of the recorded volume.

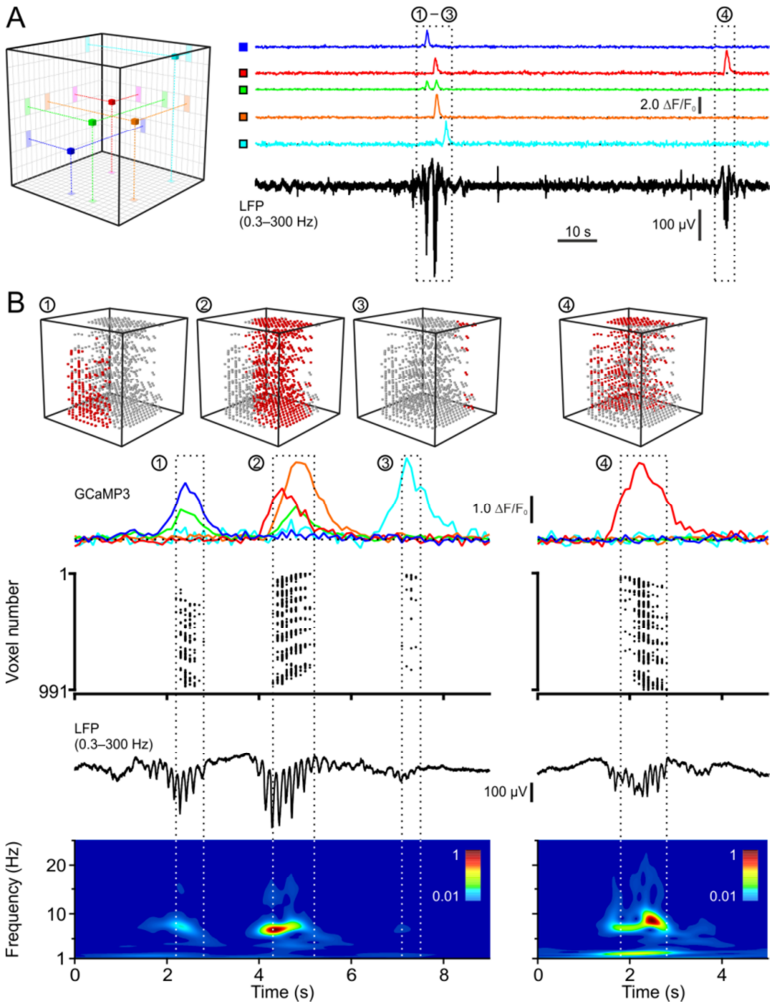

Figure 12. Spatiotemporally confined spontaneous network activity in neonatal visual cortex *in vivo*. (A) Left: Individual voxels projected in 3D space (500 × 500 × 200 μm^3). Right: Sample traces (ΔF/F0) of GCaMP3 fluorescence (color code refers to voxels on the left) and time-aligned LFP signal (filtered at 0.3–300 Hz). Detected Ca^{2+} clusters are indicated by encircled numbers. Boxed regions are shown at higher magnification in B. (B) Top row: 3D reconstruction of Ca^{2+} clusters (numbers refer to those in A). Only scanned voxels are displayed (red — active, gray — inactive). 2nd to 5th row: Time-aligned sample traces of GCaMP3 fluorescence for voxels shown in A, raster plot displaying times of peaks of all analyzed voxels, LFP signal (0.3–300 Hz) and Morlet wavelet spectrum. Modified from (Kummer et al. 2016).

Simultaneous extracellular recordings provide electrophysiological correlation of the observed Ca^{2+} clusters. It was found that 95.1% of detected calcium clusters (n = 370, data from three mice) were correlated with distinct local field potential (LFP) signals (Fig. 12A). In the majority of cases (93.5%, n = 352 Ca^{2+} clusters), they correlated with spindle-shaped oscillations with peak frequency in theta range (4–8 Hz), as shown by wavelet-based time-frequency analysis (Fig. 12B, bottom row). These electro-physiological characteristics are in agreement with those of previously reported spindle bursts in the neonatal rodent visual cortex (Kirmse et al. 2015, Hanganu et al. 2007, Hanganu et al. 2006).
In conclusion, spontaneous network activity in visual cortex is spatially confined, reflected as 3D columnar Ca^{2+} clusters in imaging recordings.

4.2.8 Wide-field calcium imaging of spontaneous network activity in the neonatal visual cortex *in vivo*

Although the 3D voxel-based two-photon Ca^{2+} imaging technique provides detailed spatiotemporal information of the on-going spontaneous network activity, the maximum recording time turned out to be limited by photo-bleaching. One-photon wide-field epi-fluorescence imaging (Kirmse et al. 2015) enables longer recording times.
As for methodological validation, paired wide-field Ca^{2+} imaging (with a 10× objective) and LFP recording (~300 kΩ, glass electrode, 0–6000 Hz) were performed from $Emx1^{IREScre}$:$GCaMP3^{LSL}$ animals at P3–4 (Fig. 13A). The recording was performed in the continuous presence of nitrous oxide. The field of view for wide-field imaging was 1.134×0.867 mm. Wide-field imaging data analysis was performed on a regular (17×13) grid of quadratic regions of interests (ROIs). Unbiased peak detection of spontaneous Ca^{2+} transients was carried out per ROI using a template matching algorithm (Kirmse et al. 2015). Based on the detected peaks of Ca^{2+} transients, a temporal criterion was applied for the definition of Ca^{2+} clusters. The paired recording showed that the detected Ca^{2+} transients were paralleled by spindle bursts, similar to the 3D voxel two-photon recordings. Therefore, wide-field imaging is suitable for the detection of correlated cortical activity *in vivo*.

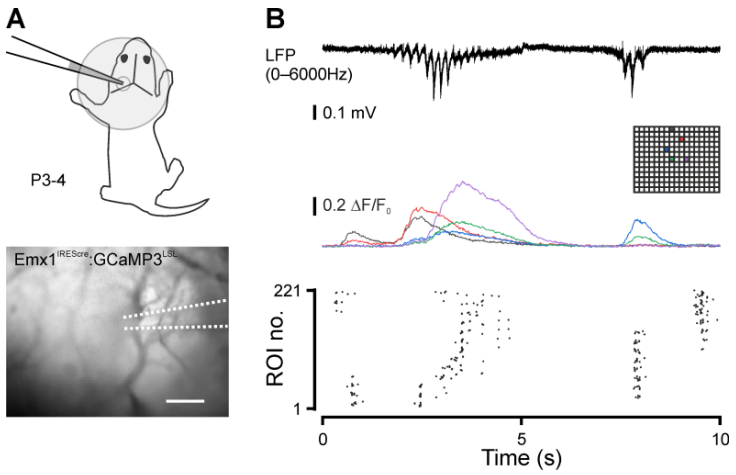

Figure 13. Wide-field calcium imaging of correlated network activity in the neonatal visual cortex *in vivo*. A, Experimental scheme (up) and typical field of view with a glass extracellular recording electrode inserted from an Emx1^{IREScre}:GCaMP3^{LSL} animal at the age of P3–4 (scale bar, 200 µm). B, Sample extracellular recording (up), sample calcium traces (middle) from insets indicated ROIs and raster plots demonstrating cluster activity – analysis was performed on a regular (17×13) grid of quadratic regions of interests. Raster plot of detected calcium transient peaks.

4.2.9 The generation of correlated network activity in the neonatal visual cortex *in vivo* is independent of NKCC1

It was next explored whether NKCC1 contributes to the generation of correlated network activity in the neonatal visual cortex *in vivo*. Since cGDPs were mainly detected at P5–9 in somatosensory cortex *in vitro* (Allene et al. 2008) and spontaneous network activity in visual cortex undergoes dramatic developmental changes during the first two postnatal weeks (Colonnese and Khazipov 2010, Colonnese et al. 2010), the current study focused on two sequential time points, namely P3–4 and P9–10. Wide-field imaging recordings were performed from both GCaMP3 NKCC1 WT and GCaMP3 NKCC1 KO^{Emx1} animals at the age of P3–4 in the continuous presence of nitrous oxide. It was found that the mean frequency of Ca^{2+} transients per ROI did not significantly differ between recordings from GCaMP3 NKCC1 WT and GCaMP3 NKCC1 KO^{Emx1} animals (WT: 2.48 ± 0.04 min^{-1}, n = 6 animals, KO^{Emx1}: 2.48 ± 0.14 min^{-1}, n = 7 animals, t(7.05) = –5.4 × 10^{-4}, P = 1.0, Welch's t-test, Fig. 14B). In addition, cluster frequency and cluster area (defined as percentage of active ROIs per cluster) were not significantly different between recordings from GCaMP3 NKCC1 WT and GCaMP3 NKCC1 KO^{Emx1} animals either

(cluster frequency, WT: 19.7 ± 1.3 min^{-1}, n = 6 animals, KO^{Emx1}: 21.7 ± 1.1 min^{-1}, n = 7 animals, t(11) = –1.20, P = 0.25, two-sample t-test, Fig. 14D, cluster area, WT: 12.8 ± 0.7 %, n = 6 animals, KO^{Emx1}: 11.5 ± 0.7 %, n = 7 animals, t(11) = 1.33, P = 0.21, two-sample t-test, Fig. 14C). These results were in line with previously published work, in which NKCC1 was acutely blocked by bumetanide perfusion through the intact dura mater (Kirmse et al. 2015). Next wide-field imaging at the age of P9–10 was performed. At this age, it was found that the mean frequency per ROI was also not significantly different between recordings from GCaMP3 NKCC1 WT and GCaMP3 NKCC1 KO^{Emx1} animals (WT: 9.6 ± 0.3 min^{-1}, n = 7 animals, NKCC1 KO^{Emx1}: 8.9 ± 0.2 min^{-1}, n = 8 animals, U = 44, P = 0.073, Mann–Whitney U test, Fig. 14F). In addition, neither cluster frequency nor cluster area significantly differed between GCaMP3 NKCC1 WT and GCaMP3 NKCC1 KO^{Emx1} animals (Cluster frequency, WT: 41.1 ± 2.1 min^{-1}, n = 7 animals, KO^{Emx1}: 37.9 ± 1.4 min^{-1}, n = 8 animals, t(13) = 1.31, P = 0.21, two-sample t-test, Fig. 14H, cluster area, WT: 23.4 ± 1.0 %, n = 7 animals, KO^{Emx1}: 23.4 ± 0.5 %, n = 8 animals, t(13) = 0.0234, P = 0.98, two-sample t-test, Fig. 14G). These results were in line with published electrophysiological experiments using systemic injection of bumetanide (Colonnese et al. 2010). However, because wide-field calcium imaging signal gives better spatial resolution and systemically injected bumetanide poorly penetrates the BBB, therefore additionally wide-field imaging recordings were performed on $Emx1^{IREScre}$:$GCaMP3^{LSL}$ animals at the age of P9–10 with acute local superfusion of bumetanide through the intact dura mater, thereby by-passing the BBB. In agreement with data using genetic deletion of NKCC1, it was found that that mean frequency of Ca^{2+} transients per ROI was not significantly affected by bumetanide (control: 10.4 ± 0.8 min^{-1}, n = 7 animals, bumetanide: 9.9 ± 0.8 min^{-1}, n = 7 animals, t(6) = 0.648, P = 0.54, paired sample t-test, Fig. 14J). In addition, cluster frequency and cluster area did not significantly differ (cluster frequency, control: 40.2 ± 2.2 min^{-1}, n = 7 animals, bumetanide: 51.9 ± 3.1 min^{-1}, n = 7 animals, W = 6, P = 0.20, Wilcoxon test, Fig. 14L, cluster area, control: 19.4 ± 1.0 %, n = 7 animals, bumetanide: 19.1 ± 0.7 %, n = 7 animals, t(6) = 0.429, P = 0.68, paired sample t-test, Fig. 14K).

In summary, $Emx1^{IREScre}$ dependent disruption of NKCC1 or the acute pharmacological block of NKCC1 in visual cortex do not affect the generation of correlated network activity in the neonatal visual cortex *in vivo*.

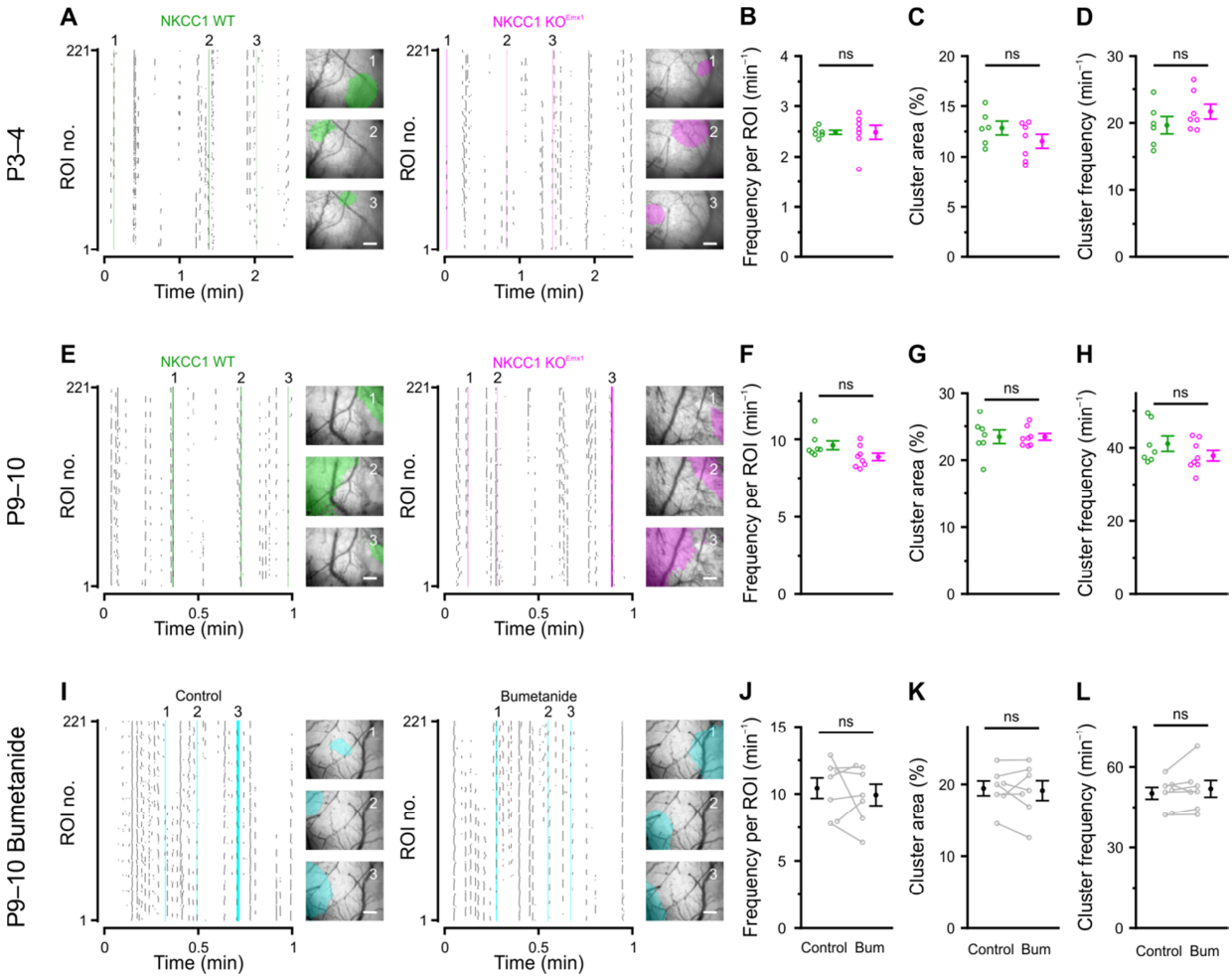

Figure 14. The generation of correlated network activity in the neonatal visual cortex *in vivo* is independent of NKCC1. A, Sample raster plots demonstrating cluster activity in the visual neocortex (P3–4) as measured through the intact skull. Transcranial GCaMP3 fluorescence overlaid with binary area plots of three spatially confined cluster events (scale bars, 200 μm). B–D, Quantification of the average frequency of Ca^{2+} transients per ROI (B), the mean cluster area as a fraction of the total size of the field of view (C) and the frequency of cluster occurrence (D). E, Sample raster plots demonstrating cluster activity in the visual neocortex (P9-10). GCaMP3 fluorescence overlaid with binary area plots of three spatially confined cluster events. F–H, Quantifications. I, Sample raster plots. J–L, Quantifications. ns – not significant.

Chapter 5. Discussion

5.1 Part 1

The main finding is that photo-stimulation with blue light – either alone or in combination with yellow light – dramatically enhances the temporal stability of eNpHR3.0-mediated currents and hence the Cl^- loading capability over a wide range of light powers. By exploiting this optimized photo-stimulation protocol, it has been demonstrated here that long-term neuronal hyperpolarization and inhibition based on eNpHR3.0 is feasible.

5.1.1 Experimental constraints related to the use of eNpHR3.0

The most relevant constraint of NpHR3.0 relies in its inactivation during continuous illumination (Zhang et al. 2007, Han and Boyden 2007), implying that NpHR3.0 is of limited value for long-lasting (>10 s) inhibition (see also Wiegert et al. 2017). However, prolonged silencing of neuronal populations is typically a critical requirement for analyzing their involvement in network oscillations and behaviors. Here, it has been demonstrated that inactivation increases with increasing light power (Fig. 4), which could be particularly problematic if expression levels are low, as is frequently the case in e.g. transgenic models. The present study reveals that inactivation is highly wavelength-dependent, being profoundly reduced for blue (488 nm) as compared to yellow (594 nm) light (Fig. 4). It should be emphasized that the degree of power-dependence of inactivation itself is much weaker for blue *versus* yellow light. This may be of great practical importance, since, within the tissue, light power declines with increasing distance from the fiber tip (Wiegert et al. 2017). Consequently, when using yellow light, cells that lie close to the light source (i.e. that are exposed to a comparatively high light power) will exhibit a more pronounced inactivation than those at greater distances. In other words, in addition to increasing the temporal stability of eNpHR3.0-mediated currents within individual cells, blue light is expected to minimize differences in inactivation kinetics between spatially distributed cells.

A general constraint of using Cl^- pumps for neuronal silencing results from a shift in E_{Cl-}, which, in turn, may induce or enhance depolarizing GABAergic/glycinergic

signaling that could counteract the eNpHR3.0-mediated hyperpolarization (Alfonsa et al. 2015, Raimondo et al. 2012). The influence of E_{Cl-} by activating eNpHR3.0 can also be used for studying the contribution of changes on E_{Cl-} to the generation of epileptic events (Alfonsa et al. 2015) as well as for studying the contribution of depolarizing GABAergic transmission to cortical network development. In fact, the magnitude of the shift in E_{Cl-} could be even enhanced by the proposed photo-stimulation protocols as they increase charge transfer for prolonged stimulation periods. That means, the optimized protocol enhances the Cl^- pumping capability of eNpHR3.0 during prolonged stimulation. However, the size of the E_{Cl-} shift can hardly be predicted, as it depends on several parameters (Cl^- extrusion capacity, resting Cl^- conductance etc.), and should be examined for each experimental setting. Additionally, due to the fast deactivation kinetics of eNpHR3.0, abrupt termination of photo-stimulation can lead to rebound depolarization and AP firing (Raimondo et al. 2012, Arrenberg et al. 2009). This effect is due to network-based mechanisms, Cl^- loading and/or activation of voltage-gated conductances (e.g. H-current, T-type Ca^{2+} current) and can be readily attenuated or abolished by replacing a step-like termination of photo-stimulation with a more gradual decrease in light power (Mahn et al. 2016).

5.1.2 Practical recommendations

Comparing continuous with high-frequency photo-stimulation regimes revealed that blue light attenuates eNpHR3.0 inactivation in a mean power-dependent manner (Fig. 3). In analogy, non-inactivating current amplitudes are largely determined by the average, rather than the peak, power of 594-nm light. These findings hence justify the use of continuous light illumination, which can be delivered using simpler hardware solutions. Largest non-inactivating currents were found for combinations with a blue light fraction of 40–60% (Fig. 4). However, as compared to photo-stimulation at 594 nm alone, use of pure blue light (488 nm) already led to a considerable increase in non-inactivating currents (Fig. 4). Furthermore, the temporal stability of eNpHR3.0-mediated currents was maximal for pure 488-nm illumination and was not further enhanced by addition of yellow light (Fig. 4).

In sum, present study provides an easy-to-implement photo-stimulation approach for the light-driven Cl^- pump eNpHR3.0 that is associated with an extraordinary temporal

stability of pump currents and hence renders eNpHR3.0 suitable for long-term neuronal inhibition and/or Cl^- loading.

5.2 Part 2

The main findings are that disruption of NKCC1 in Emx1 positive cells attenuates GABAergic depolarization and impairs spontaneous network activity in the hippocampus *in vitro* while the intrinsic excitability and maturation of basic synaptic properties are not affected, and in contrast, the generation of correlated network activity in the neonatal visual cortex *in vivo* is independent of NKCC1.

5.2.1 NKCC1 contributes to GABAergic depolarization

Several studies have examined the contribution of NKCC1 in maintaining $GABA_AR$-mediated depolarization under the pharmacological or genetic manipulation of NKCC1, either measured via gramicidin-perforated voltage patch-clamp recordings or measured via cell-attached $GABA_AR$ single channel recordings. Typical E_{GABA} values measured in neonatal neurons *in vitro* are in the range of –60 to –30 mV (Wang and Kriegstein 2011, Kirmse et al. 2010, Sipilä et al. 2006, Pfeffer et al. 2009, Nardou et al. 2009, Wang and Kriegstein 2008, Yamada et al. 2004). With gramicidin-perforated voltage-clamp technique, several studies have shown that application of the NKCC1 antagonist bumetanide shifted the E_{GABA} by –10 mV in P1–3 rat cortical neurons (Yamada et al. 2004) and by –18 mV in P2–4 rat CA3 pyramidal cells (Sipilä et al. 2006). Measurements with cell-attached single channel recording of $GABA_AR$ revealed that bumetanide shifted E_{GABA} by around –10 mV in P7–8 rat CA3 pyramidal cells. Moreover, gramicidin-perforated voltage patch-clamp recordings from two independent constitutive $NKCC1^{-/-}$ disruption studies showed that the E_{GABA} was shifted by approximately –10 mV in $NKCC1^{-/-}$ in P1 mouse CA1 pyramidal cells (Pfeffer et al. 2009) and by approximately –16 mV in $NKCC1^{-/-}$ in P3–4 mouse CA3 pyramidal cells (Sipilä et al. 2009). Gramicidin perforation allows electrical access to the intracellular compartment without destroying the barrier function of the membrane for Cl^-, however, voltage clamp recording (including gramicidin-perforated voltage-clamp) for assessing E_{GABA} requires low access resistance in order to adequately

clamp membrane potential. But gramicidin might lead to rupture of the membrane during prolonged measurement (which is typically required for gramicidin-perforated patch recording, in order to achieve low access resistance, R_a) and decrease the stability of the contact between the patch pipette and the membrane (seal resistance, R_{seal}). Due to this reason, the precision of measured E_{GABA} is then highly dependent on the quality of measurements (high quality means, without unintended rupture of membrane, with low R_a, and high R_{seal}). In addition, faithful measurement of membrane potential from immature neurons without introducing measurement artifacts is a technically challenging task. Immature neurons have high R_{input} in the gigaohm range, thus in whole-cell recordings (including gramicidin-perforated recordings), membrane potential is partly shunted through the seal which consequently leads to a depolarized measurement error (Tyzio et al. 2003). The larger the ratio of R_{input}/R_{seal}, the more prominent this shunting effect or measurement error is. To overcome the above-mentioned problems, low concentration gramicidin-perforated patch clamp recording in current mode was applied in present study to measure membrane potential and E_{GABA} (which roughly equals V_m during saturated $GABA_AR$ activation). This method could largely reduce such measurement errors, due to I) the reduced requirements of low resistance electrical access, II) the reduced risk of membrane rupture and increased seal stability by lower gramicidin concentration, (Zhu et al. 2008). In agreement with those studies, these gramicidin-perforated current clamp measurements showed around –7 mV shift in E_{GABA} (taking bicarbonate permeability into consideration, it corresponding to a shift of $[Cl^-]_{in}$ from ~17 mM to ~10 mM) between cells from WT and KO^{Emx1} animals. It should be mentioned that interestingly in those studies which have also reported about resting potential, almost all of them (Wang and Kriegstein 2011, Kirmse et al. 2010, Sipilä et al. 2009, Pfeffer et al. 2009, Nardou et al. 2009, Wang and Kriegstein 2008, Yamada et al. 2004) showed no significant influence by NKCC1 manipulation, except (Sipilä et al. 2006). In line with that, here in these recordings, resting membrane potentials recorded in cells from WT and NKCC1 KO^{Emx1} animals were not significantly different, with quite negative values (around –70 mV) and comparable with the values measured with NMDAR single channel recordings (Tyzio et al. 2003). Interestingly, in present study, after disruption of NKCC1 function, GABA is still exerting a depolarizing function. Such residual depolarization has also been observed in several other studies (Kirmse et al. 2010, Pfeffer et al. 2009, Nardou et al. 2009). A possible

explanation for the remaining depolarization in present study might be attributed to other active Cl^- loading mechanism, such as AE3 (Pfeffer et al. 2009, Gonzalez-Islas et al. 2009). Supportive evidence is: I) cells from constitutional NKCC1 knockout mice also showed remaining depolarization (Pfeffer et al. 2009); II) acute pharmacological block of NKCC1 resulted an incomplete block of GABA induced depolarization (Kirmse et al. 2010, Nardou et al. 2009), in this case, it could also be explained by incomplete depletion of $[Cl^-]_{in}$ after acute bumetanide application due to the low $GABA_AR$-mediated activity under *in vitro* conditions.
Hence with the present non-invasive measurements, one could conclude that NKCC1 contributes to GABAergic depolarization, and disruption of NKCC1 function attenuates the depolarization effect of GABA action.

5.2.2 $Emx1^{IREScre}$ dependent NKCC1 disruption does not affect synaptic maturation and intrinsic excitability

The debate on the influence of depolarizing GABA on synaptic maturation existed for a long time. On one hand, disruption of NKCC1 function in mouse by early shRNA interference or systemic pharmacological block during early development (both starting at E15) significantly reduced the spine density and hampered development of AMPAR-mediated transmission (as indicated by reduced mEPSCs frequency) (Wang and Kriegstein 2011, Wang and Kriegstein 2008). Prematurely reversing E_{GABA} via overexpression of KCC2 (E17-E18) in rat somatosensory cortex also showed impaired morphological maturation, manifested as pronounced reduction in neurite length and branch number (Cancedda et al. 2007). On the other hand, constitutive NKCC1 disruption did not impede the morphological maturation of dendrites in hippocampal cells (Pfeffer et al. 2009), and the average frequency and amplitude of mEPSCs did not differ in P5-6 CA3 pyramidal neurons (Sipilä et al. 2009). However, all the above differences might be attributed to several complicating factors, I) ubiquitous expression of NKCC1 (Kaplan et al. 1996); II) electroporation of NKCC1 shRNA and KCC2 cDNA affects only a portion of cells, in comparison to constitutive NKCC1 disruption; II) bumetanide has low BBB permeability (Wang et al. 2015, Brandt et al. 2010), IV) KCC2 contributes to the structural development of dendritic spines via interactions with the cytoskeleton (Fiumelli et al. 2013). In the $Emx1^{IREScre}$ dependent NKCC1 disruption mouse model, the unchanged frequency of $GABA_AR$

and AMPAR mediated mPSCs in hippocampus CA3 region at P3–4 and P13–14 indicates that conditional NKCC1 loss does not affect GABAergic and glutamatergic synaptic maturation, in agreement with results from constitutive NKCC1 knockout mice (Pfeffer et al. 2009, Sipilä et al. 2009). This suggests that early depolarizing GABA may not be essential for synaptic maturation. Other supportive evidence is that due to a developmental change in receptor subunit, the decay kinetics of both AMPAR mediated mEPSC and $GABA_AR$ mediated mGPSC undergo normal developmental changes, slowed down for mEPSC but accelerated for mGPSC, with no significant difference in each case between cells from WT and KO^{Emx1} animals (Wang et al. 2014, Stubblefield and Benke 2010). In contrast to the observation of unchanged mGPSC kinetics, it has been previously shown in cultured cerebellar granule cells that $[Cl^-]_{in}$ regulates the expression of α3 and α1-containing $GABA_ARs$, responsible for slow and fast decay kinetics, respectively. KCC2 induced low $[Cl^-]_{in}$ led to higher expression of α1-containing $GABA_AR$, hence faster decay kinetics (Succol et al. 2012). The discrepancy might be attributed to a difference in brain region and the difference between primary cultures and *in vivo* mouse model.

It has been shown in constitutional NKCC1 mice that loss of early depolarizing GABAergic actions led to a dramatic compensatory enhancement of intrinsic spiking of $NKCC1^{-/-}$ cells measured at P6–7 (Sipilä et al. 2009). In their study, the intrinsic spiking frequency was sixfold higher in $NKCC1^{-/-}$ cells (~1.9 Hz) compared with WT cells (~0.3 Hz). In contrast to that, with the same cell-attached recording method, the present data showed that at P3–4 $Emx1^{IREScre}$ dependent disruption of NKCC1 does not alter the intrinsic excitability in $NKCC1^{-/-}$ cells, the measured intrinsic spiking frequency from NKCC1 KO^{Emx1} and WT animals are both around 0.3 Hz. With whole-cell recording, it was here found that neither are passive properties nor is AP threshold significantly different between cells from WT and NKCC1 KO^{Emx1} animals. Hence, the intrinsic excitability is not affected by $Emx1^{IREScre}$ dependent NKCC1 disruption. The underlying reason for the discrepancy remained unclear, however the conditional knockout model ruled out possible peripheral effects which might be caused by non-CNS knockout of NKCC1.

5.2.3 Differential contribution of depolarizing GABA to network activity

The depolarizing action of GABA has been consistently shown in different cortex areas during the early stage of development. It is therefore expected that, at network level, GABAergic transmission should have a promoting effect for the generation of spontaneous correlated network activity. Indeed, the pharmacological NKCC1 inhibitor bumetanide blocks GDPs in the hippocampus and cGDPs in somatosensory cortex *in vitro* (Pfeffer et al. 2009, Nardou et al. 2009, Allene et al. 2008). In line with these studies, it was here found that Emx1^{IREScre} dependent disruption of NKCC1 impairs spontaneous correlated network activity in the hippocampus *in vitro* as reflected by reduced sGPSC bursts in slices from NKCC1 KO^{Emx1} animals. In addition, another set of experiment utilizing the optogenetic tool eNpHR3.0 revealed that loading Cl^- specifically in Emx1 positive cells can rescue the bumetanide-sensitive sPSC bursts in neonatal hippocampus CA3 region. Present data provided causal evidence that depolarizing GABA contributes to the generation of spontaneous correlated network activity, and also showed that manipulating depolarizing GABA in the pyramidal cell population alone is sufficient to cause corresponding changes in network activity. Moreover, the observation of unaltered synaptic maturation and intrinsic excitability suggest that this impaired generation of correlated hippocampal network activity *in vitro* is due to a shift in E_{Cl-}.

Despite the clear promotion effect of depolarizing GABA on network activity under *in vitro* conditions, supportive *in vivo* evidence is virtually absent. Several lines of evidence suggest that depolarizing GABA is not contributing to the generation of spontaneous network activity in the neocortex *in vivo* (Kirmse et al. 2015, Minlebaev et al. 2007). A recent *in vivo* study showed that application of the NKCC1 antagonist bumetanide through the intact dura mater does not affect the generation of spontaneous network activity (as reflected by unaffected Ca^{2+} cluster frequency and size in wide-field recordings) in visual cortex at P3–4, despite a depolarizing effect of GABA action *in vivo* (Kirmse et al. 2015). Another *in vivo* study performed in somatosensory cortex at P2–7 showed that bumetanide perfusion (dura was cut and removed) does not affect the occurrence and the spectral characteristics of spontaneous spindle-bursts as measured by using multi-electrode arrays (Minlebaev et al. 2007). In contrast, another *in vivo* study revealed that intraperitoneal application of bumetanide blocks early hippocampus sharp waves (SPWs) (measured by the use

of LFP recordings) in a reversible manner (Sipilä et al. 2006). These studies are of valuable, however, the pharmacological approach has its limitation. Concerns for these studies are the uncertainty about effective penetration depth of bumetanide, the concentration dependent specificity of bumetanide, and the non-CNS block of NKCC1. The $Emx1^{IREScre}$ dependent NKCC1 disruption enables us to circumvent these problems. The non-invasive wide-field *in vivo* measurements revealed no significant difference on visual cortex spontaneous network activity between WT and NKCC1 KO^{Emx1} animals on two sequential developmental stages (P3–4 and P9–10), as the measured calcium cluster frequency and size are not significant different between genotypes. These data are in line with previous studies (Kirmse et al. 2015, Minlebaev et al. 2007) and suggest that the generation of correlated network activity in the neonatal visual cortex *in vivo* is independent of NKCC1 mediated depolarizing GABA.

It is worth to mention that, applying non-invasive cell-attached recording method, the GABA action has been directly shown to be depolarizing at single cellular level under *in vivo* situation (Kirmse et al. 2015). However, in the same study applying wide-field calcium imaging method GABA has been shown mainly exerting an inhibitory effect, since pharmacological block of $GABA_A$Rs led to an increased frequency and the size of Ca^{2+} clusters (Kirmse et al. 2015). This *in vitro* and *in vivo* discrepancy was also demonstrated by Valeeva and colleagues with an optogenetic strategy. They selectively expressed channelrhodopsin-2 in GABAergic interneurons and recorded glutamatergic PSCs (EPSCs), which served as a measure of the firing activity of presynaptic glutamatergic neurons. They showed that during early development EPSC frequency was increased by stimulation of GABAergic interneurons in the immature hippocampus and neocortex *in vitro*, but reduced *in vivo* (Valeeva et al. 2016). This discrepancy might be explained by an activity-dependent change in E_{GABA} and a difference in resting membrane potential under *in vitro* and *in vivo* conditions (Kirmse and Holthoff 2017, Valeeva et al. 2016, Kirmse et al. 2015).

In summary, NKCC1-mediated depolarizing GABA contributes to the generation of hippocampal spontaneous network activity *in vitro* but does not affect spontaneous cortex activity under *in vivo* conditions in neonatal animals.

5.2.4 Biological purpose of the GABAergic depolarization

The novel Emx1^{IREScre} dependent NKCC1 knockout mouse model allowed us to access the developmental importance of depolarizing GABA for the generation of cortical network activity. Here, it was observed that disruption of NKCC1 in Emx1 positive cells attenuates depolarizing GABA, however, does not affect the synaptic maturation and intrinsic excitability. Interestingly, the attenuated depolarizing GABA leads to an impaired generation of spontaneous network activity in hippocampus *in vitro,* while the generation of spontaneous network activity in visual cortex *in vivo* is independent of NKCC1. In the past years, emerging evidence shows that $GABA_AR$ signaling appears to be inhibitory at network lever throughout postembryonic development, despite the depolarizing effect at single cellular level (Kirmse et al. 2015, Han et al. 2015, Minlebaev et al. 2007, Lamsa et al. 2000). The fact that depolarizing GABA does neither influence synaptic maturation nor the generation of spontaneous network activity *in vivo* lead us to think why are immature neurons have high $[Cl^-]_{in}$ which promotes $GABA_AR$-dependent depolarization? It is frequently overlooked that a low $[Cl^-]_{in}$ represents a specialization of mature neurons and, at the same time, an exceptional case in cell biology (Kirmse et al. 2018, Kirmse and Holthoff 2017). From an evolutionary point of view, neuron network development should be optimized for energy consumption. Actually, a hyperpolarizing mode of GABA action is energetically more expensive compared to depolarizing GABA action (Kirmse and Holthoff 2017, Doyon et al. 2016, Kaila et al. 2014, Buzsaki et al. 2007), since ATP consumption in order to maintain potassium homeostasis for a neuron is higher for Cl^- extrusion through KCC2 compared with Cl^- loading by NKCC1 (Doyon et al. 2016). There are two interesting facts: I) immature neuron network has a low level of ongoing network activity; II) activation of $GABA_AR$ exert shunting inhibition regardless of the mode of GABA action, and potency of shunting inhibition is negatively correlated with $[Cl^-]_{in}$. These facts indicate that neuron network does not require strong inhibition. Therefore one could speculate that in order to reduce overall energy consumption, Cl^- is loaded actively as an optimization during neuron network development. Because by doing this neuron could maximally preserve depolarizing effect of glutamatergic transmission while keeping network under safe control, in other words, free from over-excitation. This view is supported by recent theoretical simulation work as well (Rahmati et al. 2017). Moreover, the increasing need of

inhibition is accompanied by a developmental decrease of $[Cl^-]_{in}$ as this would render shunting inhibition stronger (Doyon et al. 2016) and expression of $GABA_BR$, which enables modification of excitability though inwardly rectifying potassium channels.

Chapter 6. Conclusions

6.1 Part 1

The inhibitory optogenetic actuator eNpHR3.0 is limited for applications that require prolonged inhibition, due to the pronounced decline of photo-current over time. To overcome this limitation, photo-stimulation regimes have been systematically optimized and it was found that blue light excitation profoundly increases the stability of eNpHR3.0-mediated currents during long-term photo-stimulation. The optimized approach enables stable neuronal silencing on a time-scale of minutes, thereby extending the spectrum of applications to situations in which long-lasting inhibition of neuronal activity and Cl^- loading is required.

6.2 Part 2

Immature cortical neurons have elevated $[Cl^-]_{in,}$ which causes $GABA_AR$ activation to be depolarizing. To explore the role of depolarizing GABAergic transmission for cortical network development, a conditional NKCC1 (major Cl^- importer) knockout mouse model was used. Here, utilizing patch-clamp techniques, it was found that $Emx1^{IREScre}$ dependent NKCC1 disruption attenuates depolarizing GABA and impairs the generation of spontaneous correlated network activity in the hippocampus *in vitro*. Novel application of optogenetic tool eNpHR3.0 to artificially load Cl^- in Emx1 positive cells further provided causal evidence that depolarizing GABA contributes to the generation of spontaneous network activity *in vitro*. However, the network dynamic change is neither due to an altered intrinsic excitability nor due to a change in synaptic maturation, but attributed to an attenuated NKCC1 mediated depolarizing GABA. Further, with the use of *in vivo* wide-field imaging technique, it was found that disruption of NKCC1 in Emx1 positive cells does not affect the development of spontaneous network activity in the visual cortex. In conclusion, NKCC1-mediated depolarizing action of GABA is not required for major aspects of cortical network development, although it does contribute to the generation of spontaneous network activity in the hippocampus *in vitro*.

References

Airan RD, Thompson KR, Fenno LE, Bernstein H, Deisseroth K. 2009. Temporally precise in vivo control of intracellular signalling. Nature, 458 (7241):1025-1029.

Alfonsa H. 2015. Optogenetic chloride loading in neurons: implications for epilepsy.

Alfonsa H, Merricks EM, Codadu NK, Cunningham MO, Deisseroth K, Racca C, Trevelyan AJ. 2015. The contribution of raised intraneuronal chloride to epileptic network activity. J Neurosci, 35 (20):7715-7726.

Allene C, Cattani A, Ackman JB, Bonifazi P, Aniksztejn L, Ben-Ari Y, Cossart R. 2008. Sequential generation of two distinct synapse-driven network patterns in developing neocortex. J Neurosci, 28 (48):12851-12863.

Antoine MW, Hübner CA, Arezzo JC, Hebert JM. 2013. A Causative Link Between Inner Ear Defects and Long-Term Striatal Dysfunction. Science, 341 (6150):1120-1123.

Arrenberg AB, Del Bene F, Baier H. 2009. Optical control of zebrafish behavior with halorhodopsin. Proceedings of the National Academy of Sciences of the United States of America, 106 (42):17968-17973.

Austin S, Ziese M, Sternberg N. 1981. A novel role for site-specific recombination in maintenance of bacterial replicons. Cell, 25 (3):729-736.

Bamberg E, Tittor J, Oesterhelt D. 1993. Light-Driven Proton or Chloride Pumping by Halorhodopsin. Proceedings of the National Academy of Sciences of the United States of America, 90 (2):639-643.

Barry PH, Lynch JW. 1991. Liquid junction potentials and small cell effects in patch-clamp analysis. J Membr Biol, 121 (2):101-117.

Berndt A, Lee SY, Wietek J, Ramakrishnan C, Steinberg EE, Rashid AJ, Kim H, Park S, Santoro A, Frankland PW, Iyer SM, Pak S, Ahrlund-Richter S, Delp SL, Malenka RC, Josselyn SA, Carlen M, Hegemann P, Deisseroth K. 2016. Structural foundations of optogenetics: Determinants of channelrhodopsin ion selectivity. Proc Natl Acad Sci U S A, 113 (4):822-829.

Bormann J, Hamill OP, Sakmann B. 1987. Mechanism of Anion Permeation through Channels Gated by Glycine and Gamma-Aminobutyric-Acid in Mouse Cultured Spinal Neurons. Journal of Physiology-London, 385:243-286.

Brandt C, Nozadze M, Heuchert N, Rattka M, Löscher W. 2010. Disease-modifying effects of phenobarbital and the NKCC1 inhibitor bumetanide in the pilocarpine model of temporal lobe epilepsy. J Neurosci, 30 (25):8602-8612.

Bui AD, Alexander A, Soltesz I. 2017. Seizing Control: From Current Treatments to Optogenetic Interventions in Epilepsy. Neuroscientist, 23 (1):68-81.

Buzsaki G, Kaila K, Raichle M. 2007. Inhibition and brain work. Neuron, 56 (5):771-783.

Cancedda L, Fiumelli H, Chen K, Poo MM. 2007. Excitatory GABA action is essential for morphological maturation of cortical neurons in vivo. J Neurosci, 27 (19):5224-5235.

Chow BY, Han X, Dobry AS, Qian X, Chuong AS, Li M, Henninger MA, Belfort GM, Lin Y, Monahan PE, Boyden ES. 2010. High-performance genetically targetable optical neural silencing by light-driven proton pumps. Nature, 463 (7277):98-102.

Colonnese MT, Khazipov R. 2010. "Slow activity transients" in infant rat visual cortex: a spreading synchronous oscillation patterned by retinal waves. J Neurosci, 30 (12):4325-4337.

Colonnese MT, Kaminska A, Minlebaev M, Milh M, Bloem B, Lescure S, Moriette G, Chiron C, Ben-Ari Y, Khazipov R. 2010. A conserved switch in sensory processing prepares developing neocortex for vision. Neuron, 67 (3):480-498.
Deidda G, Allegra M, Cerri C, Naskar S, Bony G, Zunino G, Bozzi Y, Caleo M, Cancedda L. 2015. Early depolarizing GABA controls critical-period plasticity in the rat visual cortex. Nat Neurosci, 18 (1):87-96.
Delpire E, Lu J, England R, Dull C, Thorne T. 1999. Deafness and imbalance associated with inactivation of the secretory Na-K-2Cl co-transporter. Nat Genet, 22 (2):192-195.
Doyon N, Vinay L, Prescott SA, De Koninck Y. 2016. Chloride Regulation: A Dynamic Equilibrium Crucial for Synaptic Inhibition. Neuron, 89 (6):1157-1172.
Dusterwald KM, Currin CB, Burman RJ, Akerman CJ, Kay AR, Raimondo JV. 2018. Biophysical models reveal the relative importance of transporter proteins and impermeant anions in chloride homeostasis. Elife, 7.
Fiumelli H, Briner A, Puskarjov M, Blaesse P, Belem BJ, Dayer AG, Kaila K, Martin JL, Vutskits L. 2013. An ion transport-independent role for the cation-chloride cotransporter KCC2 in dendritic spinogenesis in vivo. Cereb Cortex, 23 (2):378-388.
Földy C, Lee SH, Morgan RJ, Soltesz I. 2010. Regulation of fast-spiking basket cell synapses by the chloride channel ClC-2. Nat Neurosci, 13 (9):1047-1049.
Garaschuk O, Milos RI, Konnerth A. 2006. Targeted bulk-loading of fluorescent indicators for two-photon brain imaging in vivo. Nature Protocols, 1 (1):380-386.
Glykys J, Dzhala V, Egawa K, Balena T, Saponjian Y, Kuchibhotla KV, Bacskai BJ, Kahle KT, Zeuthen T, Staley KJ. 2014. Local impermeant anions establish the neuronal chloride concentration. Science, 343 (6171):670-675.
Göbel W, Kampa BM, Helmchen F. 2007. Imaging cellular network dynamics in three dimensions using fast 3D laser scanning. Nature Methods, 4 (1):73-79.
Gonzalez-Islas C, Chub N, Wenner P. 2009. NKCC1 and AE3 appear to accumulate chloride in embryonic motoneurons. J Neurophysiol, 101 (2):507-518.
Gorski JA, Talley T, Qiu M, Puelles L, Rubenstein JL, Jones KR. 2002. Cortical excitatory neurons and glia, but not GABAergic neurons, are produced in the Emx1-expressing lineage. J Neurosci, 22 (15):6309-6314.
Gradinaru V, Zhang F, Ramakrishnan C, Mattis J, Prakash R, Diester I, Goshen I, Thompson KR, Deisseroth K. 2010. Molecular and Cellular Approaches for Diversifying and Extending Optogenetics. Cell, 141 (1):154-165.
Gulledge AT, Stuart GJ. 2003. Excitatory actions of GABA in the cortex. Neuron, 37 (2):299-309.
Han B, Bellemer A, Koelle MR. 2015. An evolutionarily conserved switch in response to GABA affects development and behavior of the locomotor circuit of Caenorhabditis elegans. Genetics, 199 (4):1159-1172.
Han X, Boyden ES. 2007. Multiple-Color Optical Activation, Silencing, and Desynchronization of Neural Activity, with Single-Spike Temporal Resolution. Plos One, 2 (3).
Hanganu IL, Ben-Ari Y, Khazipov R. 2006. Retinal waves trigger spindle bursts in the neonatal rat visual cortex. J Neurosci, 26 (25):6728-6736.
Hanganu IL, Staiger JF, Ben-Ari Y, Khazipov R. 2007. Cholinergic modulation of spindle bursts in the neonatal rat visual cortex in vivo. J Neurosci, 27 (21):5694-5705.

Hendry SH, Schwark HD, Jones EG, Yan J. 1987. Numbers and proportions of GABA-immunoreactive neurons in different areas of monkey cerebral cortex. J Neurosci, 7 (5):1503-1519.
Hübner CA, Holthoff K. 2013. Anion transport and GABA signaling. Front Cell Neurosci, 7:177.
Jacob TC, Moss SJ, Jurd R. 2008. GABA(A) receptor trafficking and its role in the dynamic modulation of neuronal inhibition. Nat Rev Neurosci, 9 (5):331-343.
Jentsch TJ, Stein V, Weinreich F, Zdebik AA. 2002. Molecular structure and physiological function of chloride channels. Physiol Rev, 82 (2):503-568.
Jin X, Huguenard JR, Prince DA. 2005. Impaired Cl− extrusion in layer V pyramidal neurons of chronically injured epileptogenic neocortex. Journal of neurophysiology, 93 (4):2117-2126.
Kaila K, Voipio J, Paalasmaa P, Pasternack M, Deisz RA. 1993. The role of bicarbonate in GABAA receptor-mediated IPSPs of rat neocortical neurones. J Physiol, 464:273-289.
Kaila K, Ruusuvuori E, Seja P, Voipio J, Puskarjov M. 2014. GABA actions and ionic plasticity in epilepsy. Curr Opin Neurobiol, 26:34-41.
Kang HJ, Kawasawa YI, Cheng F, Zhu Y, Xu X, Li M, Sousa AM, Pletikos M, Meyer KA, Sedmak G, Guennel T, Shin Y, Johnson MB, Krsnik Z, Mayer S, Fertuzinhos S, Umlauf S, Lisgo SN, Vortmeyer A, Weinberger DR, Mane S, Hyde TM, Huttner A, Reimers M, Kleinman JE, Sestan N. 2011. Spatio-temporal transcriptome of the human brain. Nature, 478 (7370):483-489.
Kaplan MR, Mount DB, Delpire E. 1996. Molecular mechanisms of NaCl cotransport. Annu Rev Physiol, 58:649-668.
Khalilov I, Dzhala V, Ben-Ari Y, Khazipov R. 1999. Dual role of GABA in the neonatal rat hippocampus. Dev Neurosci, 21 (3-5):310-319.
Khazipov R, Luhmann HJ. 2006. Early patterns of electrical activity in the developing cerebral cortex of humans and rodents. Trends Neurosci, 29 (7):414-418.
Kim JM, Hwa J, Garriga P, Reeves PJ, RajBhandary UL, Khorana HG. 2005. Light-driven activation of beta 2-adrenergic receptor signaling by a chimeric rhodopsin containing the beta 2-adrenergic receptor cytoplasmic loops. Biochemistry, 44 (7):2284-2292.
Kirmse K, Holthoff K. 2017. Functions of GABAergic transmission in the immature brain. e-Neuroforum, 23 (1).
Kirmse K, Witte OW, Holthoff K. 2010. GABA depolarizes immature neocortical neurons in the presence of the ketone body ss-hydroxybutyrate. J Neurosci, 30 (47):16002-16007.
Kirmse K, Witte OW, Holthoff K. 2011. GABAergic depolarization during early cortical development and implications for anticonvulsive therapy in neonates. Epilepsia, 52 (9):1532-1543.
Kirmse K, Hübner CA, Isbrandt D, Witte OW, Holthoff K. 2018. GABAergic Transmission during Brain Development: Multiple Effects at Multiple Stages. Neuroscientist, 24 (1):36-53.
Kirmse K, Kummer M, Kovalchuk Y, Witte OW, Garaschuk O, Holthoff K. 2015. GABA depolarizes immature neurons and inhibits network activity in the neonatal neocortex in vivo. Nat Commun, 6:7750.
Klapper SD, Swiersy A, Bamberg E, Busskamp V. 2016. Biophysical Properties of Optogenetic Tools and Their Application for Vision Restoration Approaches. Frontiers in Systems Neuroscience, 10.

Kummer M, Kirmse K, Witte OW, Holthoff K. 2012. Reliable in vivo identification of both GABAergic and glutamatergic neurons using Emx1-Cre driven fluorescent reporter expression. Cell Calcium, 52 (2):182-189.
Kummer M, Kirmse K, Witte OW, Haueisen J, Holthoff K. 2015. Method to quantify accuracy of position feedback signals of a three-dimensional two-photon laser-scanning microscope. Biomed Opt Express, 6 (10):3678-3693.
Kummer M, Kirmse K, Zhang CQ, Haueisen J, Witte OW, Holthoff K. 2016. Column-like Ca2+ clusters in the mouse neonatal neocortex revealed by three-dimensional two-photon Ca2+ imaging in vivo. Neuroimage, 138:64-75.
Lamsa K, Palva JM, Ruusuvuori E, Kaila K, Taira T. 2000. Synaptic GABA(A) activation inhibits AMPA-kainate receptor-mediated bursting in the newborn (P0-P2) rat hippocampus. J Neurophysiol, 83 (1):359-366.
Löscher W, Puskarjov M, Kaila K. 2013. Cation-chloride cotransporters NKCC1 and KCC2 as potential targets for novel antiepileptic and antiepileptogenic treatments. Neuropharmacology, 69:62-74.
Luhmann HJ, Sinning A, Yang JW, Reyes-Puerta V, Stuttgen MC, Kirischuk S, Kilb W. 2016. Spontaneous Neuronal Activity in Developing Neocortical Networks: From Single Cells to Large-Scale Interactions. Front Neural Circuits, 10:40.
Madisen L, Mao T, Koch H, Zhuo JM, Berenyi A, Fujisawa S, Hsu YW, Garcia AJ, 3rd, Gu X, Zanella S, Kidney J, Gu H, Mao Y, Hooks BM, Boyden ES, Buzsaki G, Ramirez JM, Jones AR, Svoboda K, Han X, Turner EE, Zeng H. 2012. A toolbox of Cre-dependent optogenetic transgenic mice for light-induced activation and silencing. Nat Neurosci, 15 (5):793-802.
Mahn M, Prigge M, Ron S, Levy R, Yizhar O. 2016. Biophysical constraints of optogenetic inhibition at presynaptic terminals. Nature Neuroscience, 19 (4):554-556.
Mason MJ, Simpson AK, Mahaut-Smith MP, Robinson HP. 2005. The interpretation of current-clamp recordings in the cell-attached patch-clamp configuration. Biophys J, 88 (1):739-750.
Masseck OA, Spoida K, Dalkara D, Maejima T, Rubelowski JM, Wallhorn L, Deneris ES, Herlitze S. 2014. Vertebrate cone opsins enable sustained and highly sensitive rapid control of Gi/o signaling in anxiety circuitry. Neuron, 81 (6):1263-1273.
Mattis J, Tye KM, Ferenczi EA, Ramakrishnan C, O'Shea DJ, Prakash R, Gunaydin LA, Hyun M, Fenno LE, Gradinaru V, Yizhar O, Deisseroth K. 2012. Principles for applying optogenetic tools derived from direct comparative analysis of microbial opsins. Nature Methods, 9 (2):159-172.
Micheva KD, Beaulieu C. 1996. Quantitative aspects of synaptogenesis in the rat barrel field cortex with special reference to GABA circuitry. J Comp Neurol, 373 (3):340-354.
Minlebaev M, Ben-Ari Y, Khazipov R. 2007. Network mechanisms of spindle-burst oscillations in the neonatal rat barrel cortex in vivo. J Neurophysiol, 97 (1):692-700.
Moser T. 2015. Optogenetic stimulation of the auditory pathway for research and future prosthetics. Curr Opin Neurobiol, 34:29-36.
Nardou R, Ben-Ari Y, Khalilov I. 2009. Bumetanide, an NKCC1 Antagonist, Does Not Prevent Formation of Epileptogenic Focus but Blocks Epileptic Focus Seizures in Immature Rat Hippocampus. Journal of Neurophysiology, 101 (6):2878-2888.
Owens DF, Boyce LH, Davis MB, Kriegstein AR. 1996. Excitatory GABA responses in embryonic and neonatal cortical slices demonstrated by gramicidin

perforated-patch recordings and calcium imaging. J Neurosci, 16 (20):6414-6423.
Perkins KL. 2006. Cell-attached voltage-clamp and current-clamp recording and stimulation techniques in brain slices. J Neurosci Methods, 154 (1-2):1-18.
Pfeffer CK, Stein V, Keating DJ, Maier H, Rinke I, Rudhard Y, Hentschke M, Rune GM, Jentsch TJ, Hübner CA. 2009. NKCC1-dependent GABAergic excitation drives synaptic network maturation during early hippocampal development. J Neurosci, 29 (11):3419-3430.
Plotkin MD, Snyder EY, Hebert SC, Delpire E. 1997. Expression of the Na-K-2Cl cotransporter is developmentally regulated in postnatal rat brains: A possible mechanism underlying GABA's excitatory role in immature brain. Journal of Neurobiology, 33 (6):781-795.
Price GD, Trussell LO. 2006. Estimate of the chloride concentration in a central glutamatergic terminal: a gramicidin perforated-patch study on the calyx of Held. J Neurosci, 26 (44):11432-11436.
Rahmati V, Kirmse K, Holthoff K, Schwabe L, Kiebel SJ. 2017. Developmental Emergence of Sparse Coding: A Dynamic Systems Approach. Sci Rep, 7 (1):13015.
Raimondo JV, Kay L, Ellender TJ, Akerman CJ. 2012. Optogenetic silencing strategies differ in their effects on inhibitory synaptic transmission. Nature Neuroscience, 15 (8):1102-1104.
Ratte S, Prescott SA. 2011. ClC-2 channels regulate neuronal excitability, not intracellular chloride levels. J Neurosci, 31 (44):15838-15843.
Rheims S, Minlebaev M, Ivanov A, Represa A, Khazipov R, Holmes GL, Ben-Ari Y, Zilberter Y. 2008. Excitatory GABA in rodent developing neocortex in vitro. J Neurophysiol, 100 (2):609-619.
Rinke I, Artmann J, Stein V. 2010. ClC-2 voltage-gated channels constitute part of the background conductance and assist chloride extrusion. J Neurosci, 30 (13):4776-4786.
Rivera C, Voipio J, Payne JA, Ruusuvuori E, Lahtinen H, Lamsa K, Pirvola U, Saarma M, Kaila K. 1999. The K+/Cl- co-transporter KCC2 renders GABA hyperpolarizing during neuronal maturation. Nature, 397 (6716):251-255.
Sipilä ST, Schuchmann S, Voipio J, Yamada J, Kaila K. 2006. The cation-chloride cotransporter NKCC1 promotes sharp waves in the neonatal rat hippocampus. J Physiol, 573 (Pt 3):765-773.
Sipilä ST, Huttu K, Yamada J, Afzalov R, Voipio J, Blaesse P, Kaila K. 2009. Compensatory enhancement of intrinsic spiking upon NKCC1 disruption in neonatal hippocampus. J Neurosci, 29 (21):6982-6988.
Siuda ER, McCall JG, Al-Hasani R, Shin G, Il Park S, Schmidt MJ, Anderson SL, Planer WJ, Rogers JA, Bruchas MR. 2015. Optodynamic simulation of beta-adrenergic receptor signalling. Nat Commun, 6:8480.
Spruston N. 2009. Dendritic signal integration.
Stein V, Nicoll RA. 2003. GABA generates excitement. Neuron, 37 (3):375-378.
Stein V, Hermans-Borgmeyer I, Jentsch TJ, Hübner CA. 2004. Expression of the KCl cotransporter KCC2 parallels neuronal maturation and the emergence of low intracellular chloride. J Comp Neurol, 468 (1):57-64.
Stubblefield EA, Benke TA. 2010. Distinct AMPA-type glutamatergic synapses in developing rat CA1 hippocampus. J Neurophysiol, 104 (4):1899-1912.
Succol F, Fiumelli H, Benfenati F, Cancedda L, Barberis A. 2012. Intracellular chloride concentration influences the GABAA receptor subunit composition. Nat Commun, 3:738.

Sulis Sato S, Artoni P, Landi S, Cozzolino O, Parra R, Pracucci E, Trovato F, Szczurkowska J, Luin S, Arosio D, Beltram F, Cancedda L, Kaila K, Ratto GM. 2017. Simultaneous two-photon imaging of intracellular chloride concentration and pH in mouse pyramidal neurons in vivo. Proc Natl Acad Sci U S A, 114 (41):E8770-E8779.

Szabadics J, Varga C, Molnar G, Olah S, Barzo P, Tamas G. 2006. Excitatory effect of GABAergic axo-axonic cells in cortical microcircuits. Science, 311 (5758):233-235.

Tonnesen J, Sorensen AT, Deisseroth K, Lundberg C, Kokaia M. 2009. Optogenetic control of epileptiform activity. Proceedings of the National Academy of Sciences of the United States of America, 106 (29):12162-12167.

Tyzio R, Ivanov A, Bernard C, Holmes GL, Ben-Ari Y, Khazipov R. 2003. Membrane potential of CA3 hippocampal pyramidal cells during postnatal development. J Neurophysiol, 90 (5):2964-2972.

Tyzio R, Minlebaev M, Rheims S, Ivanov A, Jorquera I, Holmes GL, Zilberter Y, Ben-Ari Y, Khazipov R. 2008. Postnatal changes in somatic gamma-aminobutyric acid signalling in the rat hippocampus. Eur J Neurosci, 27 (10):2515-2528.

Tyzio R, Allene C, Nardou R, Picardo MA, Yamamoto S, Sivakumaran S, Caiati MD, Rheims S, Minlebaev M, Milh M, Ferre P, Khazipov R, Romette JL, Lorquin J, Cossart R, Khalilov I, Nehlig A, Cherubini E, Ben-Ari Y. 2011. Depolarizing actions of GABA in immature neurons depend neither on ketone bodies nor on pyruvate. J Neurosci, 31 (1):34-45.

Valeeva G, Tressard T, Mukhtarov M, Baude A, Khazipov R. 2016. An Optogenetic Approach for Investigation of Excitatory and Inhibitory Network GABA Actions in Mice Expressing Channelrhodopsin-2 in GABAergic Neurons. J Neurosci, 36 (22):5961-5973.

Wang DD, Kriegstein AR. 2008. GABA regulates excitatory synapse formation in the neocortex via NMDA receptor activation. J Neurosci, 28 (21):5547-5558.

Wang DD, Kriegstein AR. 2011. Blocking Early GABA Depolarization with Bumetanide Results in Permanent Alterations in Cortical Circuits and Sensorimotor Gating Deficits. Cerebral Cortex, 21:574-587.

Wang H, Megill A, Wong PC, Kirkwood A, Lee HK. 2014. Postsynaptic target specific synaptic dysfunctions in the CA3 area of BACE1 knockout mice. PLoS One, 9 (3):e92279.

Wang S, Zhang XQ, Song CG, Xiao T, Zhao M, Zhu G, Zhao CS. 2015. In Vivo Effects of Bumetanide at Brain Concentrations Incompatible with Nkcc1 Inhibition on Newborn Dgc Structure and Spontaneous Eeg Seizures Following Hypoxia-Induced Neonatal Seizures. Neuroscience, 286:203-215.

Wiegert JS, Mahn M, Prigge M, Printz Y, Yizhar O. 2017. Silencing Neurons: Tools, Applications, and Experimental Constraints. Neuron, 95 (3):504-529.

Wietek J, Beltramo R, Scanziani M, Hegemann P, Oertner TG, Wiegert JS. 2015. An improved chloride-conducting channelrhodopsin for light-induced inhibition of neuronal activity in vivo. Sci Rep, 5:14807.

Wright R. 2009. The necessity of NKCC1: loss of the chloride cotransporter in a knock-out model and potential compensatory mechanisms. J Neurosci, 29 (42):13094-13096.

Yamada J, Okabe A, Toyoda H, Kilb W, Luhmann HJ, Fukuda A. 2004. Cl- uptake promoting depolarizing GABA actions in immature rat neocortical neurones is mediated by NKCC1. J Physiol, 557 (Pt 3):829-841.

Zariwala HA, Borghuis BG, Hoogland TM, Madisen L, Tian L, De Zeeuw CI, Zeng H, Looger LL, Svoboda K, Chen TW. 2012. A Cre-dependent GCaMP3 reporter mouse for neuronal imaging in vivo. J Neurosci, 32 (9):3131-3141.

Zhang F, Wang LP, Brauner M, Liewald JF, Kay K, Watzke N, Wood PG, Bamberg E, Nagel G, Gottschalk A, Deisseroth K. 2007. Multimodal fast optical interrogation of neural circuitry. Nature, 446 (7136):633-U634.

Zhang F, Vierock J, Yizhar O, Fenno LE, Tsunoda S, Kianianmomeni A, Prigge M, Berndt A, Cushman J, Polle J, Magnuson J, Hegemann P, Deisseroth K. 2011. The Microbial Opsin Family of Optogenetic Tools. Cell, 147 (7):1446-1457.

Zhu L, Polley N, Mathews GC, Delpire E. 2008. NKCC1 and KCC2 prevent hyperexcitability in the mouse hippocampus. Epilepsy Res, 79 (2-3):201-212.

Ehrenwörtliche Erklärung

Hiermit erkläre ich, dass mir die Promotionsordnung der Medizinischen Fakultät der Friedrich-Schiller-Universität bekannt ist,
ich die Dissertation selbst angefertigt habe und alle von mir benutzten Hilfsmittel, persönlichen Mitteilungen und Quellen in meiner Arbeit angegeben sind,
mich folgende Personen bei der Auswahl und Auswertung des Materials sowie bei der Herstellung des Manuskripts unterstützt haben:

PD Dr. med. habil. Knut Kirmse
BioImaging, Hans-Berger-Klinik für Neurologie, Universitätsklinikum Jena
Wesentlicher Beitrag zum Design der Experimente, der Datenanalyse, der Vorbereitung der Abbildungen und Erstellung beider Manuskripte, deren Ergebnisse, Text und Zahlen in den Absätzen 4.1.1 bis 4.1.4, 4.2.2 – 4.2.6 und 4.2.8 – 4.2.9 modifiziert und erweitert wurden (Manuskripte in Vorbereitung).
Wesentlicher Beitrag zum Design der Experimente, der Datenanalyse, der Vorbereitung der Abbildungen und Erstellung des Manuskripts, dessen Ergebnisse, Text und Zahlen im Absatz 4.2.7 modifiziert und erweitert wurden (Kummer et al. 2016).

Univ.-Prof. Dr. rer. nat. Knut Holthoff
BioImaging, Hans-Berger-Klinik für Neurologie, Universitätsklinikum Jena
Wesentlicher Beitrag zum Design der Experimente, der Interpretation der Ergebnisse der vorliegenden Arbeit und dem Anfertigen des Manuskripts (Kummer et al. 2016).

Prof. Dr. med. Otto W. Witte
Hans-Berger-Klinik für Neurologie, Universitätsklinikum Jena
Unterstützung bei der Interpretation der Ergebnisse der vorliegenden Arbeit und dem Anfertigen des Manuskripts (Kummer et al. 2016).

Prof. Dr.-Ing. habil. Jens Haueisen
Institute of Biomedical Engineering and Informatics,
Technical University Ilmenau
Unterstützung beim Aufbau des 2-Photonen-Spiralscansystems und dem Anfertigen des Manuskripts (Kummer et al. 2016).

Dr.-Ing. Michael Kummer
BioImaging, Hans-Berger-Klinik für Neurologie, Universitätsklinikum Jena
Unterstützung beim Aufbau des 2-Photonen-Spiralscansystems und dem Anfertigen des Manuskripts (Kummer et al. 2016).

Tom Floßmann
BioImaging, Hans-Berger-Klinik für Neurologie, Universitätsklinikum Jena
Durchführung von Vorversuchen zur Optimierung des eNpHR3.0-Stimulus, die nicht im endgültigen Manuskript enthalten sind.

Magdalena Aurelia Otto
BioImaging, Hans-Berger-Klinik für Neurologie, Universitätsklinikum Jena
Unterstützung für die Verbesserung und Validierung der Vorlage für die Erkennung von Calcium-Transienten, die für Daten von P9-10-Tieren verwendet wurde.

Ina Ingrisch
Hans-Berger-Klinik für Neurologie, Universitätsklinikum Jena
Durchführung der Genotypisierung.

Sindy Beck
Hans-Berger-Klinik für Neurologie, Universitätsklinikum Jena
Durchführung der Genotypisierung.

die Hilfe eines Promotionsberaters nicht in Anspruch genommen wurde und dass Dritte weder unmittelbar noch mittelbar geldwerte Leistungen von mir für Arbeiten erhalten haben, die im Zusammenhang mit dem Inhalt der vorgelegten Dissertation stehen,

dass ich die Dissertation noch nicht als Prüfungsarbeit für eine staatliche oder andere wissenschaftliche Prüfung eingereicht habe und

dass ich die gleiche, eine in wesentlichen Teilen ähnliche oder eine andere Abhandlung nicht bei einer anderen Hochschule als Dissertation eingereicht habe.

Jena 29.1.2019 — Zhang Chuangiang

Ort, Datum — Unterschrift des Verfassers

Publications

Kummer M, Kirmse K, Zhang CQ, Haueisen J, Witte OW, Holthoff K. 2016. Column-like Ca2+ clusters in the mouse neonatal neocortex revealed by three-dimensional two-photon Ca2+ imaging *in vivo*. Neuroimage, 138:64-75.

Wang XH, Wu Y, Yang XF, Miao Y, Zhang CQ, Dong LD, Yang XL, Wang Z. 2016. Cannabinoid CB1 receptor signaling dichotomously modulates inhibitory and excitatory synaptic transmission in rat inner retina. Brain Struct Funct, 221 (1):301-316.

Zhang CQ, Wu HJ, Wang SY, Yin S, Lu XJ, Miao Y, Wang XH, Yang XL, Wang Z. 2013. Suppression of outward K(+) currents by WIN55212-2 in rat retinal ganglion cells is independent of CB1/CB2 receptors. Neuroscience, 253:183-193.